Journal of Nanobiotechnology

RESEARCH

Open Access

Multitargeted nanoparticles inhibit cancer invasion by disrupting cancer-associated fibroblast-tumor cell crosstalk and modulating collagen pattern and EMT

Liting Wang[1†], Pei Zhi[1†], Ibrahim Alradwan[1,2], Chunsheng He[1], Azhar Z. Abbasi[1], Han Gao[1], Andrew M. Rauth[3], David W. Cescon[4], Jeffrey T. Henderson[1] and Xiao Yu Wu[1*]

Abstract

Background Cancer-associated fibroblasts (CAFs), a major component of tumor stroma, play an important role in tumor progression and metastasis *via* paracrine signaling, extracellular matrix (ECM) remodelling, and the secretion of growth factors, cytokines, and chemokines promoting tumor growth. In this study, we aim to develop a multitargeted nanoparticle formulation to simultaneously target CAFs and triple negative breast cancer (TNBC) cells, aiming to block their crosstalk, remodel the ECM, and inhibit epithelial-mesenchymal transition (EMT) to suppress tumor growth and metastatic processes.

Methods The potential of CAFs as therapeutic target for TNBC was evaluated by analyzing RNA-seq data from TNBC patients. A novel iRGD-functionalized polymer-lipid hybrid nanoparticle (iRGD-DOX-oHA-PLN) was specifically designed to target αvβ3 and αvβ5 receptors on both tumor cells and CAFs. A murine TNBC cell line and its orthotopic in vivo model were used for efficacy evaluation. Within this model, a murine fibroblast cell line was incorporated as a source of CAFs for in vitro investigation of the crosstalk between CAFs and tumor cells. In addition, the mechanism of iRGD-DOX-oHA-PLN nanoparticles in disrupting CAF-tumor cell interactions by blocking downstream features associated with metastases including paracrine communication, collagen organization and epithelial-mesenchymal transition (EMT) associated with metastasis were investigated both in vitro and in vivo.

Results The iRGD-DOX-oHA-PLN demonstrates higher cellular uptake and cytotoxicity in CAFs overexpressing integrins αvβ3 and αvβ5 compared to normal fibroblasts. The results demonstrate that iRGD-DOX-oHA-PLN significantly restricts the interaction of CAFs and cancer cells, due to interruption of paracrine communication induced by pro-metastatic TGF-β and CXCL12 secretion together with a reduction of CXCR4 expression. Consistent with the in vitro results, in an orthotopic syngeneic TNBC murine model, iRGD-DOX-oHA-PLN effectively depletes

[†]Liting Wang and Pei Zhi contributed equally to this work.

*Correspondence:
Xiao Yu Wu
sxy.wu@utoronto.ca

Full list of author information is available at the end of the article

CAFs, reducing tumor-associated collagen production, and altering tumor-associated collagen signatures (TACS). Thus, iRGD-DOX-oHA-PLN treatment impedes tumor invasion by reducing MMP-9 secretion and inhibiting EMT.

Conclusion The data reveals that simultaneously targeting CAFs and tumor cells, while blocking their crosstalk *via* application of a multitargeted nanomedicine, offers a compelling and effective strategy to inhibit metastasis of TNBC.

Keywords Cancer-associated fibroblast (CAF), CAF-cancer interactions, Tumor microenvironment, Triple negative breast cancer, Multitargeted nanoparticles, Tumor-associated collagen signatures, Epithelial-mesenchymal transition

Graphical Abstract

Wang et al

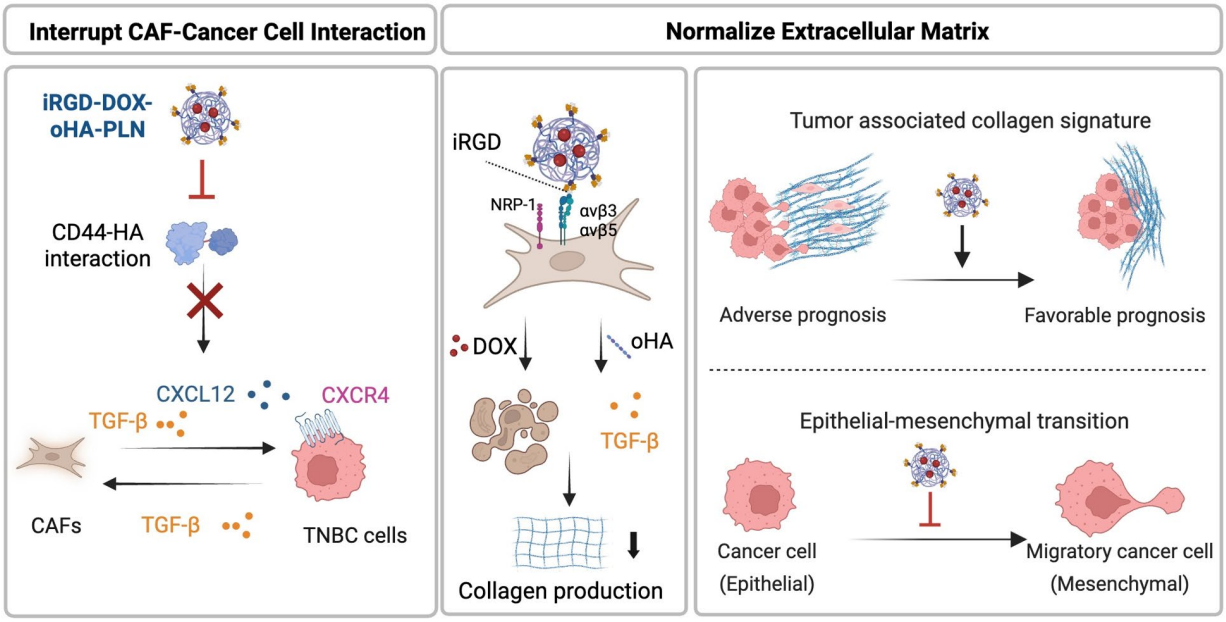

Introduction

Breast cancer is widely recognized as the most common malignant tumor in women worldwide. Among various subtypes, triple-negative breast cancer (TNBC) constitutes approximately 10% to 15% of all breast cancers [1]. TNBC exhibits aggressive tumor growth in the absence of estrogen receptor (ER), progesterone receptor (PR) and human epidermal growth factor receptor 2 (HER2) expression. This, combined with the highly heterogeneous nature of TNBC, poses challenges in understanding the underlying disease biology of TNBC, limiting the effectiveness of targeted therapies [2]. Among patients receiving standard immunotherapy combined with chemotherapy, recurrence rates remain high [3, 4]. As cancer treatments advance beyond cancer cell-centered approaches, there is a growing emphasis on understanding and targeting the tumor microenvironment (TME). Among various tumor stromal cells, cancer-associated fibroblasts (CAFs) are particularly abundant and have been shown to play a key role in modulating tumor progression and metastasis [5]. In TNBC tumors, up to 80% of fibroblasts adopt an altered cancer phenotype, often characterized by increased expression of α-smooth muscle actin (α-SMA), fibroblast activation protein (FAP), and upregulation of cytokines such as transforming growth factor-β (TGF-β) and interleukin-6 (IL-6) [6–8].

Despite the ongoing debate regarding the dual roles of CAFs in potentially promoting and inhibiting cancer invasion, most studies agree that the presence of CAFs play a critical role in facilitating treatment resistance and cancer metastasis through direct interaction with cancer cells [9]. Specifically, entrapped CAFs produce growth factors, chemokines, cytokines, and other small molecules contributing to carcinogenesis, angiogenesis, tumor invasion, and immunosuppression [10–13]. For example, CAF-derived TGF-β interacts with cancer cell receptors, promoting the EMT by inducing loss of their polarity and enhancing motility. The CXC-chemokine ligand 12 (CXCL12) produced by CAFs can engage with

C-X-C chemokine receptor type 4 (CXCR4) in cancer cells, promoting cancer cell proliferation [10]. Through its secretion of CXCL12, CAFs can impede recruitment and activation of T lymphocytes while promoting the recruitment of immunosuppressive cells to suppress anti-tumor immunity [14]. Beyond their interaction with cancer cells *via* paracrine communication, another distinct function of CAFs is their ability to construct and remodel the extracellular matrix (ECM). As reported, CAFs can synthesize excessive ECM components, especially fibrillar collagens (type I, III, IV and V) and hyaluronan (HA), promoting tumor proliferation and metastasis [15]. Among these collagens, particularly type I which through aberrant deposition and alignment, increases ECM stiffness activating multiple pathways to support the proliferation and invasion of tumor cells [16]. The organization and alignment of collagen, also known as tumor-associated collagen signatures (TACS), actively influence tumor behavior and clinical outcomes [17]. In this respect, type I collagen serves as a diagnostic biomarker of metastasis and as a prognostic indicator, its expression being positively correlated with poorer clinical outcomes in breast cancer. The underlie mechanisms of this phenomenon is varied and complex, suggesting type I collagen aids in promoting tumor progression and metastasis, including phosphoinositide 3-kinase (PI3K)-Akt and TGF-β dependent pathways [18]. With respect to the ECM, HA also plays a pivotal role in regulating tumor progression. The overproduction of HA (> 1000 kDa) seen in CAFs not only structurally supports tumor growth, but also enhances tumor cell invasion by interacting with its receptor - cluster of differentiation 44 (CD44) and the receptor for hyaluronic acid mediated motility (RHAMM), to upregulate signaling cascades including the mitogen-activated protein kinase/extracellular-signal-regulated kinase (MAPK/ERK) pathway and the PI3K-Akt pathway. Additionally, CAFs can produce matrix degradation molecules such as matrix metalloproteinases (MMPs) to induce EMT and reduce cell adhesion, ultimately facilitating the migration of cancer cells [19]. Therefore, targeting the CAFs and CAF-derived factors might be a promising strategy to achieve anti-tumoral effect.

To simultaneously suppress CAF-cancer cell signaling relevant to cell invasion, we developed a novel αvβ3/αvβ5-targeted polymer-lipid hybrid nanoparticles (PLN) system (iRGD-DOX-oHA-PLN) in order to synergistically deliver the chemotherapeutic doxorubicin (DOX) and oligomeric HA (oHA, < 10 kDa) to tumor sites (Scheme 1). To do this, an internalizing RGD (iRGD: sequence CRGDKGPDC) was used to enhance internalization of nanoparticles into both TNBC cells and CAFs *via* recognition of αvβ3 and αvβ5 and their subsequent binding to neuropilin-1 (NRP-1) [20, 21]. In this approach, targeted delivery of oHA suppresses proliferation and metastasis of TNBC by competitively binding to CD44, thereby blocking CD44-HA interactions [21–23]. As a result, oHA inhibits paracrine communication between CAFs and cancer cells by suppressing TGF-β generation and CXCL12/CXCR4 signaling. To normalize the aberrant ECM, the iRGD-DOX-oHA-PLN depletes CAFs, reduces collagen production and altering TACS playing a significant role in regulating cancer behavior and prognosis. This system also impedes cell invasion by reducing MMP production to suppress the EMT. Collectively, iRGD-DOX-oHA-PLNs significantly disrupts the pro-tumoral crosstalk between CAFs and cancer cells, regulating collagen and inhibiting the EMT; ultimately suppressing tumor progression and metastasis. These findings highlight the potent anti-tumor effects of iRGD-DOX-oHA-PLN by targeting and regulating multiple components of the TME, indicating a potential therapeutic strategy for TNBC.

Materials and methods

Reagents

Polyoxyethylene (40) stearate (Myrj 52), N-(3-dimethylaminopropyl)-N′-ethylcarbodiimide hydrochloride (EDC), N-hydroxysuccinimide (NHS), poly-2-hydroxyethyl methacrylate (poly-HEMA), and all other chemicals were purchased from Sigma-Aldrich Canada (Oakville, ON, Canada). Ethyl arachidate was purchased from TCI America (Portland, OR, USA). Polyoxyethylene (100) stearate (Myrj 59) was purchased from Spectrum Chemical (Gardena, CA, USA). Cyclic peptide iRGD [c(CRGDRGPDC)] was purchased from LifeTein (Somerset, NJ, USA). Pluronic-F 68 was purchased from BASF Corporation (Parsippany, NJ, USA). Doxorubicin hydrochloride was purchased from MedChemExpress (Monmouth Junction, NJ, USA). oHA (~7 kDa) was purchased from Bloomage Biochem Co., Ltd. (Shandong, China). D-Luciferin was purchased from Cayman Chemicals (Ann Arbor, MI, USA). Cyanine5 amine was purchased from Lumiprobe Corporation (Hunt Valley, MD, USA). Anti-β-actin (ab8226), anti-αv (ab179475), anti-αSMA (ab5694), anti-CXCR4 (ab124824), anti-vimentin (ab92547) antibodies, goat anti-mouse IgG H&L (HRP) (ab6789), goat anti-rabbit IgG H&L (HRP) (ab205718), goat anti-rabbit IgG H&L (Alexa Fluor® 594) (ab150080), and goat anti-mouse IgG H&L (Alexa Fluor® 488) (ab150113) were purchased from Abcam (Cambridge, UK). The β3 antibody (13166 S), β5 antibody (3629 S), and anti-collagen I antibody (72026 S) were purchased from Cell Signaling Technology (Boston, MA, USA). The anti-MMP-9 antibody (sc-13520) was purchased from Santa Cruz Biotechnology (Dallas, TX, USA). The anti-FAPα antibody (MSB9727), CXCL12/SDF-1 alpha ELISA

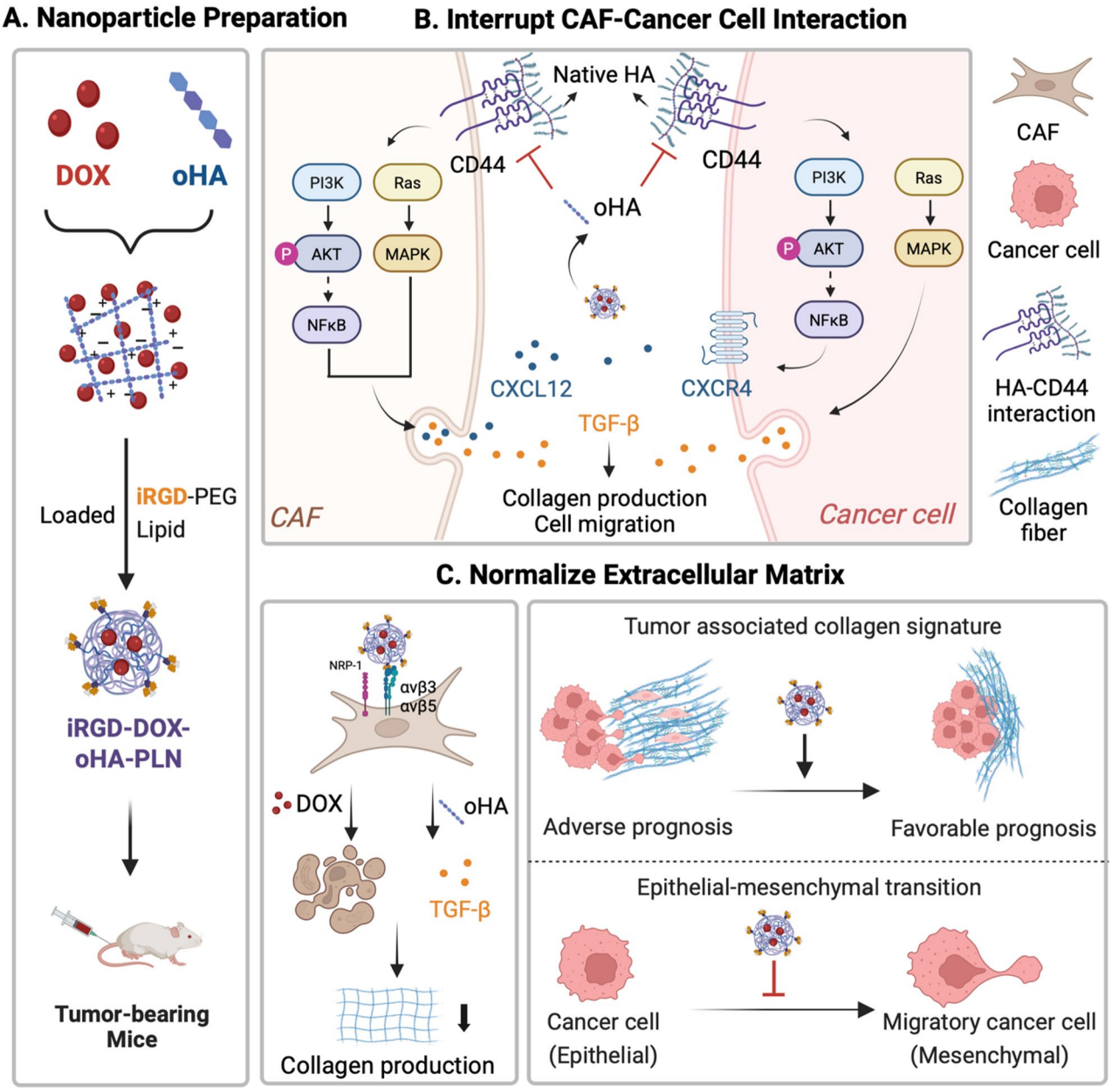

Scheme 1 Illustration of the synthesis of iRGD-DOX-oHA-PLN and its potential anti-metastatic effects *via* regulation of CAF-cancer cell crosstalk and ECM normalization. (**A**) Self-assembly of iRGD-DOX-oHA-PLN by microemulsion technology. (**B**) Mechanism of oHA-mediated blockade of CD44-HA-mediated CAF-cancer cell crosstalk. oHA released from iRGD-DOX-oHA-PLN disrupts oncogenic and pro-metastatic paracrine interactions between tumor cells and CAFs by suppressing CD44-HA signaling pathways, particularly through reduction of CXCL12 and TGF-β production and downregulation of CXCR4 expression. (**C**) Combined effects of DOX and oHA on ECM normalization by decreasing collagen production and modulating TACS. Additionally, iRGD-DOX-oHA-PLN impedes tumor cell invasion by inhibiting the EMT process

kit (MCX120), and TGF-beta 1 ELISA kit (DB100C) were purchased from R&D Systems (Minneapolis, MN, USA).

Cell lines

The murine TNBC cell line 4T1-luc (JCRB1447) supplied by the JCRB Cell Bank (Osaka, Japan), was purchased from CellBank Australia (Westmead, NSW, Australia). 4T1-luc cells were maintained in RPMI 1640 culture medium supplemented with 10% fetal bovine serum, 100 U/mL penicillin/streptomycin in a humidified atmosphere with 5% CO_2 and incubated at 37 °C.

Mouse fibroblast cell line NIH/3T3 (CRL-1658) was purchased from the American Type Culture Collection (ATCC) (Manassas, VA, USA). NIH/3T3 (abbreviated as 3T3) cells were maintained in Dulbeccos Modified Eagle Medium (DMEM) supplemented with 10% fetal bovine

serum, 100 U/mL penicillin/streptomycin in a humidified atmosphere with 5% CO_2 and at 37 °C. 3T3 cells were activated (named as a3T3 cells) to acquire CAF properties as previously described [38, 39]. Briefly, 4T1 cells were cultured in flasks until 80% confluent. Cultured media was then collected, filtered and stored at -80 °C until used. When ~ 1×10^6 3T3 cells had been grown in a T25 flask overnight, the culture media was replaced with a mixture of 50% fresh media and 50% 4T1 cell-conditioned media. The cells were then incubated for 24 h and recovered in fresh media for future experiments.

Animal models

Female BALB/c mice (6–8 weeks, 19 ± 1 g) were purchased from the Jackson Laboratory (Bar Harbor, ME, USA). They were raised under specified housing conditions (21 ± 1 ℃, 40% relative humidity and 12:12 light: dark cycle, ad libitum access to food and water). All animal experiments were conducted following Canadian Council on Animal Care guidelines and with the approval from the Animal Care Committee of the University Health Networks (UHN, Toronto, ON, Canada). To establish the orthotopic TNBC tumor model, 5×10^5 4T1-luc cells were injected into the fourth mammary fat pad of female BALB/c mice under continuous inhalation of 2% isoflurane.

Preparation and characterization of nanoparticles

DOX-oHA-PLNs were synthesized using a one-pot self-assembly method, as outlined in previous studies [21]. Briefly, ethyl arachidate (25 mg), Myrj 52 (2 mg), and Myrj 59 (1 mg) were melted at 60 ℃, followed by adding oHA (100 mg/mL, 100 µL, pH = 11.4), DOX (10 mg/mL, 250 µL), and PF-68 (100 mg/mL, 50 µL). The mixture was stirred for 20 min and sonicated for 5 min at 100% peak amplitude of cycle 1 using a probe ultrasonicator (Hielscher USA, Inc., Ringwood, NJ, USA). Then, the emulsion was quickly transferred into 2 mL of ice saline to obtain DOX-oHA-PLN. To synthesize NPs with iRGD, Myrj-iRGD instead of Myrj 59 was used, while other procedures are the same. Both HPESO and Myrj-iRGD were prepared following the previously established protocols [24, 25]. For the preparation of NPs without oHA (DOX-PLN, iRGD-DOX-PLN), hydrolyzed polymers of epoxidized soybean oil (HPESO) were used to load DOX. Nanoparticles without DOX (oHA-PLN, iRGD-oHA-PLN) were synthesized by replacing DOX with an equivalent volume of distilled deionized (DDI) water. Naked solid lipid nanoparticles (SLN) without drug loading (iRGD-SLN) were produced by replacing DOX and oHA with DDI water. In the study of cellular uptake, cyanine5 (Cy5) amine was conjugated to oHA using EDC-NHS coupling to create oHA-Cy5, which was then employed in the synthesis of iRGD-DOX-Cy5-oHA-PLN. The particle size and zeta potential of the prepared nanoparticles were measured using Malvern Zetasizer Nano ZS (Worcestershire, UK)(Data not shown). As reported in our previous work, iRGD-DOX-oHA-PLN exhibits a particle size of approximately 180 nm, a negative zeta potential of -17.5 mV, and a polydispersity index (PDI) below 0.2. The encapsulation efficiencies (EE%) of DOX and oHA are 94.76% and 81.68%, respectively [26]. TEM imaging further confirmed the spherical morphology of the iRGD-DOX-oHA-PLN. The binding affinity of iRGD-DOX-oHA-PLN and integrin was confirmed using a binding assay with recombinant human αvβ3 integrin. The colloidal stability in 5% dextrose or 50% FBS as well as storage stability of the nanoparticle formulations were also demonstrated in our previous studies [26–28].

In vitro cell viability by MTT assay

3T3 cells or a3T3 cells were seeded onto 96-well plates at a density of 1×10^4 cells/well. Following overnight incubation, cells were treated with varying concentrations of iRGD-SLN, free DOX-oHA, DOX-oHA-PLN, and iRGD-DOX-oHA-PLN and DOX concentrations of 0.01, 0.1, 0.5, 1, 5, 10 and 50 µg/mL for 24 h. Subsequently, the medium was removed, and each well was supplemented with 20 µL of MTT solution (5 mg/mL) and 80 µL of fresh medium. After incubating for 4 h at 37 ℃, the suspension was discarded, and 100 µL of DMSO was added to each well to dissolve formazan crystals. The relative cytotoxicity of each treatment group was determined by measuring absorbance at 567 nm. IC20 and IC50 values were determined using nonlinear fitting curves generated by GraphPad Prism 8.0.

Cellular uptake by spectrofluorometry

3T3 cells and a3T3 cells were seeded onto 96-well plates at a density of 1×10^4 cells/well. After overnight incubation, cells were treated with DOX-oHA-PLN and iRGD-DOX- oHA-PLN, at the DOX concentration of 1.5 µg/mL for 0.5, 1 and 2 h. At each time point, the culture media was removed and cells washed 3 × 5 min with PBS. Cells were subsequently collected and lysed with PBS containing 0.5% Triton X-100. DOX concentration was determined by fluorescence microplate assay through comparison of λex = 490 nm versus λem = 530 nm with calculations based on a preestablished standard curve.

Wound healing assay

4T1-luc cells monoculture or 4T1-luc:3T3 (1:1) were seeded into 24-well plates at a density of 2×10^5 cells per well. After 24 h adherence and proliferation, the confluent monolayer was scratched with a 200 µL pipette tip and washed with PBS three times. The remaining cells were treated with an FBS-free medium containing saline, iRGD-SLN, free oHA, oHA-PLN, and iRGD-oHA-PLN at

an equivalent oHA concentration of 10 μg/mL for 24 h. Photographs of the scratched areas will be captured at 0 h, 8 h, and 24 h after treatments. Results will be quantified using Image J software.

Transwell migration assay

4T1-luc cells and a3T3 cells were seeded into T25 flasks at a density of 5×10^5 cells. Cells were treated with saline, iRGD-SLN, free oHA, oHA-PLN, and iRGD-oHA-PLN at an equivalent oHA concentration of 10 μg/mL was performed for 24 h, followed by digestion with trypsin and transferred to the lower wells of 24-well plates in complete cell culture media. Meanwhile, a3T3 cells and 4T1-luc cells in FBS-free media were seeded into the upper chambers (8.0 μm pore polyester membrane) at a density of 5×10^4 cells. Following a 24 h migration period, cells remaining on the upper surface of the membrane were gently removed with cotton swabs. In contrast, cells that had migrated to the bottom surface were stained with a 0.5% crystal violet solution. Images capturing the migrated cells on the membrane's bottom were taken using the EVOS XL Core imaging system (Thermo Fisher Scientific, Inc., Waltham, MA, USA). Results were quantified using Image J software.

Invasion assay using co-cultured 3D spheroids

Round bottom 96-well plates were pre-coated with 100 μL of poly-HEMA (6 mg/mL) and allowed to dry overnight at room temperature in a biosafety hood. A mixture of 3T3 and 4T1-luc cells at a 10:1 ratio, totaling 2×10^3 cells were seeded onto plates. Two days post-spheroid formation, most of the media was carefully removed, and Matrigel at a final concentration of 7 mg/mL was added to encapsulate the spheroids. Growth factor-reduced Matrigel was polymerized by incubating at 37 ℃ for 30 min. Cell media containing treatments of saline, iRGD-SLN, oHA, oHA-PLN, and iRGD-oHA-PLN, all at an equivalent oHA concentration of 10 μg/mL were added. Brightfield images were then captured 4 days following treatment using the EVOS XL Core imaging system. Invasion fronts were identified using color thresholds in ImageJ.

ELISA

4T1-luc cells and a3T3 cells were cultured in 60 mm petri dishes at a density of 5×10^5 cells. The cells were treated with saline, iRGD-SLN, free oHA, oHA-PLN, and iRGD-oHA-PLN, at an equivalent oHA concentration of 10 μg/mL, for 24 h. Subsequently, the cell culture media were refreshed, and after an additional 24 h incubation period, the media were collected. These obtained media samples were then centrifuged to eliminate any cell debris. The levels of TGF-β in the supernatant were quantified using ELISA kits, following the manufacturer's instructions.

To assess the levels of TGF-β and CXCL12 in mouse tumors, female BALB/c mice with orthotopic 4T1-luc tumors were examined. Three weeks post-tumor inoculation, mice received intravenous injections of saline, DOX + oHA, DOX-oHA-PLN, or iRGD-DOX-oHA-PLN, at an equivalent DOX dose of 10 mg/kg. Three days following treatment, tumors were excised and bisected, with one half used for ELISA and the other for immunohistochemical staining. ELISA tumor samples were chopped into pieces and placed in RIPA buffer containing protease and phosphatase inhibitors. Samples were then homogenized using a homogenizer (Fisher Scientific, Ontario, Canada) and incubated for 1 h at 4 °C with mild shaking. The resulting lysates were sonicated for 20 s at 50% amplitude using a UP100H probe ultrasonicator (Hielscher Ultrasonics, Teltow, Germany). Following sonication, samples were centrifuged at 15,000 × g for 20 min at 4 °C, and the supernatants were collected. Protein concentrations were determined using the BCA assay. Aliquots of these samples were stored at -80 °C until analysis. TGF-β and CXCL12 concentrations were quantified using ELISA kits following the manufacturer's instructions.

Confocal microscopy

For cellular uptake studies, 3T3 cells and a3T3 cells were seeded onto 8-well chambered coverslips at 2×10^4 cells/well density. After overnight incubation, cells were treated with DOX-Cy5-oHA-PLN and iRGD-DOX-Cy5-oHA-PLN at intervals of 15, 30, 60, and 120 min followed by washing and fixing with 4% neutral paraformaldehyde for 15 min. Cell nuclei were stained with Hoechst 33,342 after washing for 10 min, followed by an additional 3×5 min washes with PBS before being imaged under a confocal microscope.

For the immunofluorescence analysis of FAPα and type I collagen, cells were washed 3 times with ice-cold PBS post-treatment and then fixed with 4% neutralized paraformaldehyde for 15 min. The cells were then processed through the following steps: (1) blocking and permeabilization with PBS containing 5% bovine serum albumin (BSA) and 0.3% Triton X-100 for 1 h, (2) incubation with the primary antibody diluted in PBS containing 1% BSA and 0.3% Triton X-100 for 1 h, followed by three washes with ice-cold PBS, (3) incubation with secondary antibodies for 1 h, (4) staining with Hoechst 33,342 for 10 min, and (5) three final washes with PBS before observation under a confocal microscope.

Western blotting

To assess the expression levels of integrins αv, β3, and β5, a total of 5×10^5 3T3 cells or a3T3 cells were cultured in T25 flasks overnight. Cells were then lysed using radioimmunoprecipitation assay (RIPA) buffer supplemented

with protease and phosphatase inhibitors. To maximize yield, cell lysates were subjected to sonication for 20 s at 50% pulse intensity using an ultrasonicator, followed by centrifugation to collect cell supernatants. Protein concentrations were quantified employing the bicinchoninic acid (BCA) assay. The integrins αv, β3, and β5 expression levels were subsequently determined through western blot analysis. To assess expression levels of E-cadherin, N-cadherin, MMP-9, and CXCR4, 5×10^5 4T1-luc cells were cultured in T25 flasks overnight. Cells were treated with a3T3 conditioned media saline, iRGD-SLN, free oHA, oHA-PLN, and iRGD-oHA-PLN, at an equivalent oHA concentration of 10 μg/mL, for 24 h. Specifically for CXCR4 assessment, cells received a 24-h pre-treatment with a3T3 conditioned media. Following these treatments, proteins were harvested as previously described, and the protein expression levels of E-cadherin, N-cadherin, and MMP-9 were analyzed using western blot analysis.

Immunohistochemical analysis

Samples including the fourth mammary fat pad from healthy female BALB/c mice, mouse tumors grown for 3 weeks post-inoculation, and the secondary half of tumors referenced under the "ELISA" section were collected and fixed in 10% neutral buffered formalin for 48 h followed by standard preparation into paraffin blocks. Specimens were then sectioned at 7 microns and processed for integrin (αv, β3, β5), CXCR4, α-SMA immunohistochemistry or picrosirius red staining. A component of staining procedures was carried out by the CFIBCR Histology/Microscope Core Unit (Toronto, ON, Canada). The percentage of cells or areas stained was quantified using HALO™ Image Analysis Software.

Bioinformatics analysis

The expression profiles of CAF marker (FAP) and type I collagen markers (COL1A1: collagen type I alpha 1 chain; COL1A2: collagen type I alpha 2 chain) were analyzed using R statistical computing software (version 4.3.2), drawing on RNA-seq data from The Cancer Genome Atlas (TCGA) database (cite reference https://www.cancer.gov/ccg/research/genome-sequencing/tcga), specifically for patients with ER-negative, PR-negative, and HER2-negative breast cancer. Kaplan-Meier overall survival analyses of the expression of FAP and correlation analyses were also conducted with R software (version 4.3.2), drawing on the same database. Kaplan-Meier overall survival analysis for ACTA2 (actin alpha 2) and COL1A1 was performed using the online tool kmplot.com based on mRNA gene chip data from patients with TNBC. The demographic details (including race, ethnicity, age, and other relevant characteristics) are provided in the supplementary Excel file (Supplementary Table S1).

Statistical analysis

Statistical analyses were conducted utilizing GraphPad Prism 8.0. The significance of the findings was evaluated using one-way analysis of variance (ANOVA) with Tukey's multiple comparison test correction, or *via* unpaired t-test. The data presented reflects the results of at least 3 independent experiments. Error bars denote mean ± standard deviation (S.D).

Results

Elevation of CAFs and type I collagen negatively impacts survival of TNBC patients

Previously it has been shown that the tumor stroma is crucial to cancer progression, with a higher stroma ratio in TNBC serving as a prognostic marker associated with worse overall survival and lower periods of disease-free survival [38–41]. Among stromal components, CAFs and the collagen they produce play pivotal roles in remodeling ECM and promoting metastasis, contributing to poorer clinical outcomes [41]. To evaluate the potentials of CAFs and collagen as therapeutic targets for TNBC treatment, we first analyzed the transcriptional profiles of the CAF marker FAP, together with the type I collagen synthesis genes COL1A1 and COL1A2 in TNBC patients. Notably, primary tumors from TNBC patients exhibited significantly higher levels of expression of these genes compared to normal healthy breast tissue, suggesting a dependency of this enhancement on an increased presence of CAFs and type I collagen (Fig. 1A-C). To further study whether these stromal factors directly influence survival of TNBC patients, Kaplan-Meier overall survival analysis was performed. This analysis revealed that elevated levels of CAFs and collagen are indeed associated with unfavorable clinical outcomes (Fig. 1D and E). These data suggest that targeted therapeutics for CAF may offer a promising strategy for improving TNBC patient outcomes.

Higher cellular uptake and cytotoxicity of iRGD-DOX-oHA-PLN in CAFs than in normal fibroblasts

To target CAFs within the TME, a novel αvβ3/αvβ5-targeted polymer-lipid hybrid nanoparticles system (iRGD-DOX-oHA-PLN) was developed to synergistically deliver the agents DOX and oHA. To test the efficacy of this nanoparticle, we established a murine CAF model (a3T3, which is derived from murine fibroblast line NIH/3T3) for in vitro experiments. The upregulation of FAPα on a3T3 indicated the successful induction of CAF (Fig. 2A). The western blot results demonstrated an upregulation of integrins (αv, β3, β5), which are targets of iRGD (Fig. 2B). The observed upregulation of integrins inspired us to further study the nanoparticle uptake by normal fibroblasts and CAFs. Time-dependent uptake of Cy5-labeled iRGD-DOX-oHA-PLN was observed in both

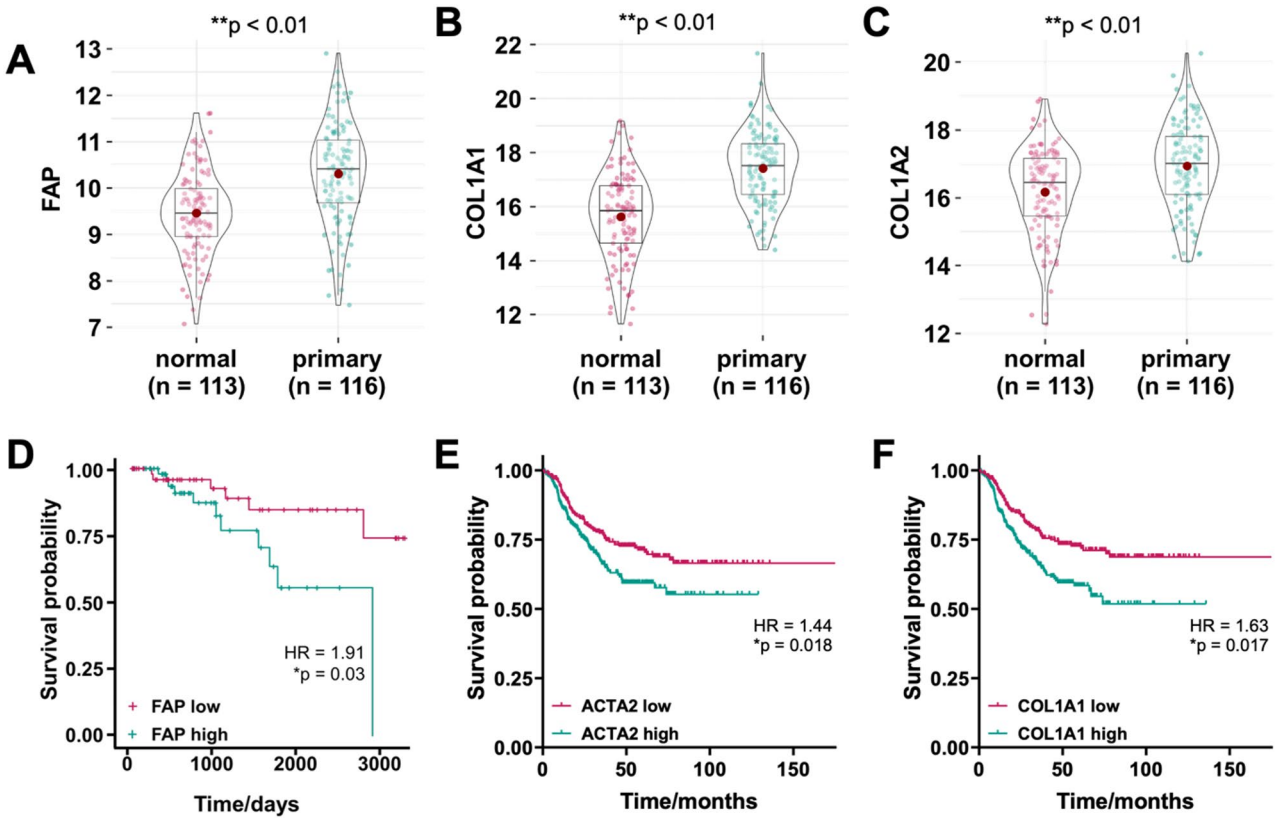

Fig. 1 CAFs and collagen are more abundant in TNBC stroma and correlate with poorer overall survival. Overexpression of (**A**) FAP, (**B**) COL1A1, and (**C**) COL1A2 are seen in TNBC patients (normal tissue, $n = 113$; primary tumor, $n = 116$). Kaplan-Meier overall survival analyses of (**D**) low and high FAP expression, (**E**) low and high ACTA2 expression, and (**F**) low and high COL1A1 expression in the tumors of TNBC patients. n (FAP low) = 58. n (FAP high) = 57. n (ACTA2 low) = 270. n (ACTA2 high) = 264. n (COL1A1 low) = 267. n (COL1A1 high) = 267. $^{*}p < 0.05$. $^{**}p < 0.01$

NIH/3T3 (3T3) and a3T3 cells, with a3T3 cells exhibiting a notably enhanced uptake and fluorescence signals for both DOX and oHA over a 2 h period (Fig. 2C and Figure S1). Moreover, iRGD-NPs showed significantly enhanced (~ 2.1-fold) cellular uptake compared to non-iRGD-NPs at 2 h in a3T3, whereas no significant difference was observed between iRGD-NPs and non-iRGD-NPs uptake in 3T3 (Fig. 2C). These findings suggest that the enhanced uptake of iRGD-NPs in a3T3 cells is facilitated by elevated αvβ3 and αvβ5 expression. The relative cytotoxicity of different treatments was then evaluated on 3T3 and a3T3 cells. The viability curves indicated that iRGD-SLN (no drug-loaded nanoparticle) exhibited only mild toxicity towards both cells (Fig. 2D). However, the IC20 values revealed a more significant inhibitory effect on a3T3 cells compared to 3T3 cells, potentially due to the attenuation of αvβ3 and αvβ5-mediated signaling. Aligning with the cellular uptake findings, iRGD-DOX-oHA-PLN showed markedly increased cytotoxicity in a3T3 relative to 3T3. Moreover, a notable reduction in IC50 values from DOX-oHA-PLN (1.97 ± 0.226 μg/mL DOX) to iRGD-DOX-oHA-PLN (0.774 ± 0.159 μg/mL DOX) treatments was only observed in a3T3 cells, emphasizing the targeted effectiveness of iRGD-DOX-oHA-PLN in CAFs compared with normal fibroblasts (Fig. 2E and F). The above finding indicates that iRGD-DOX-oHA-PLN exhibits effective enhanced cellular uptake and cytotoxicity on CAFs compared with normal fibroblasts.

Anti-migration effects observed in vitro

Both CAFs and tumor cells secrete cytokines and chemokines that activate each other, creating a positive feedback loop to promote their reciprocal migration and interaction within the TME [29–31]. This reciprocal interaction is thought to be largely driven by CD44-HA signaling. Thus, blocking this pathway may inhibit the migration of both CAFs and tumor cells [32]. To examine whether oHA-containing formulations influence cell migration *via* blockade of CD44-HA interactions, wound healing and transwell migration assays were performed and representative images are presented in Fig. 3 and Figure S2 and S3.

As shown in Fig. 3A and C, wound healing results demonstrated that co-culture of 3T3 with 4T1 cells resulted in accelerated migration of the cell mixture, exhibiting a significant increase in the migrated area by 5-fold at 8

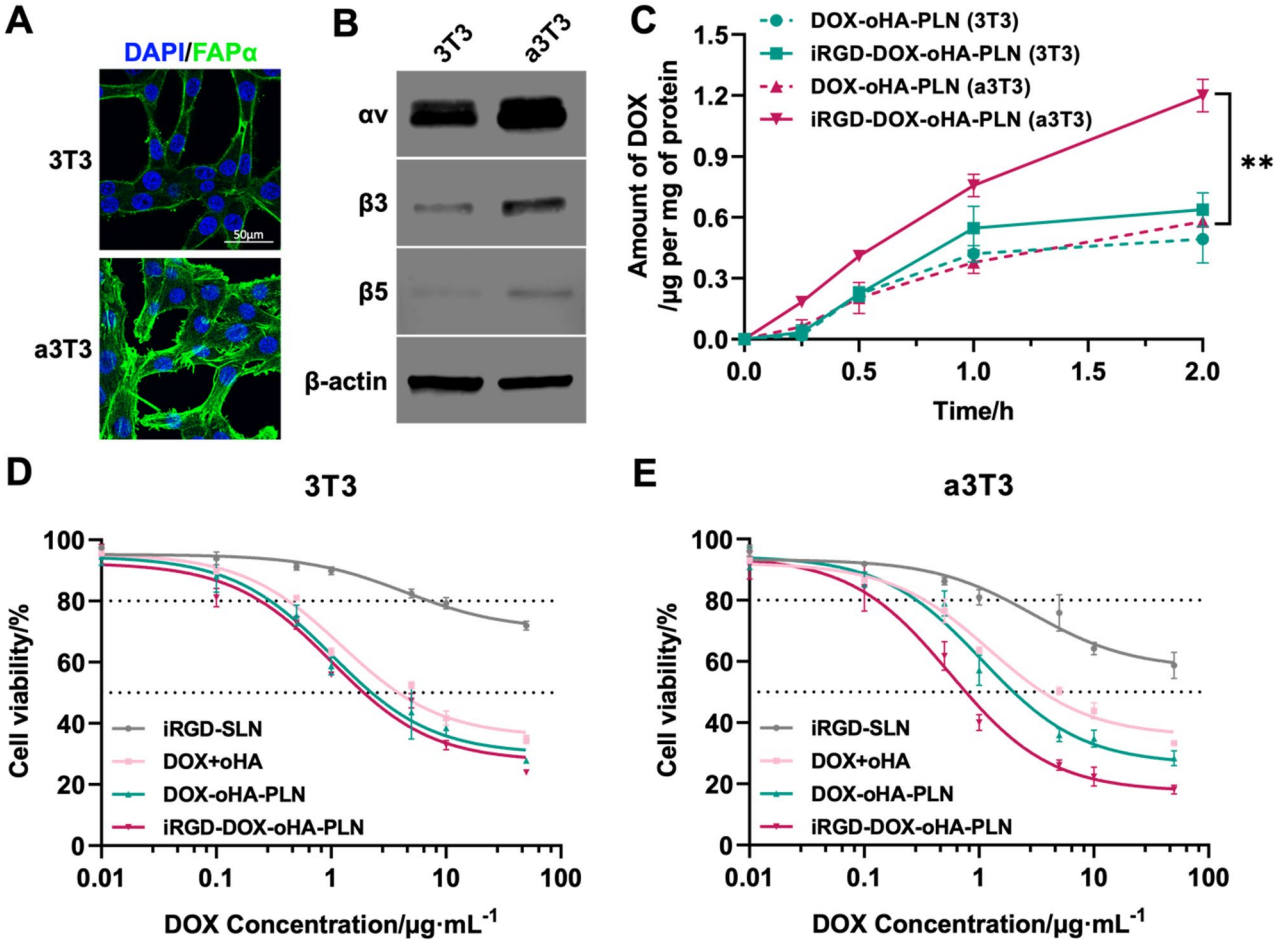

F **Table.** IC20 or IC50 values (μg·mL^{-1}) of various treatments on 3T3 and a3T3 cells

Treatments	3T3	a3T3	P Value
iRGD-SLN (IC20)	6.97 ± 0.751	1.90 ± 0.828	<0.0001 (**)
DOX+oHA	3.76 ± 0.174	3.49 ± 0.0513	0.9206
DOX-oHA-PLN	2.27 ± 0.397	1.97 ± 0.226	0.8809
iRGD-DOX-oHA-PLN	1.97 ± 0.231	0.774 ± 0.159 **	0.0177 (*)

Fig. 2 iRGD-functionalized nanoparticles demonstrated increased cellular uptake and enhanced cytotoxicity in activated mouse fibroblasts than normal mouse fibroblasts. (**A**) Confocal microscopic images show fibroblast activation protein α (FAPα) expression in 3T3 cells and a3T3 cells. Scale bar = 50 μm (**B**) Western blot images of integrins αv, β3, β5 and β-actin in 3T3 cells and a3T3 cells. (**C**) Fold increase in the internalized DOX fluorescence signal in 3T3 cells and a3T3 cells after being treated with DOX-oHA-PLN and iRGD-DOX-oHA-PLN ([DOX] = 1.5 μg/mL) for up to 2 h evaluated by a spectrofluorometer. The measured DOX concentrations were normalized to cellular protein concentrations. $n = 3$. Dose-response curve of (**D**) 3T3 cells and (**E**) activated 3T3 cells after being treated with iRGD-SLN, free DOX-oHA, DOX-oHA-PLN, and iRGD-DOX-oHA-PLN at DOX concertation of 0.01–50 μg/mL (mass ratio of DOX: oHA = 1:4) for 24 h. $n = 3$. (**F**) IC20 values (equivalent to μg/mL DOX) of iRGD-SLN or IC50 values (μg/mL DOX) of drug-containing treatments on 3T3 and a3T3 cells. Data are presented as mean ± SD. *$p < 0.05$. **$p < 0.01$

h and 1.7-fold at 24 h, compared to 4T1 cell monocultures. Such effects highlight the role of CAF in facilitating cancer cell migration. When treating the co-cultured 4T1 and 3T3 cells with iRGD-SLN and oHA-containing formulations, the cell migration was markedly inhibited at 8 h. By 24 h, all treatments significantly suppressed cell motility relative to the saline control, with the effectiveness in the following order: iRGD-oHA-PLN > oHA-PLN

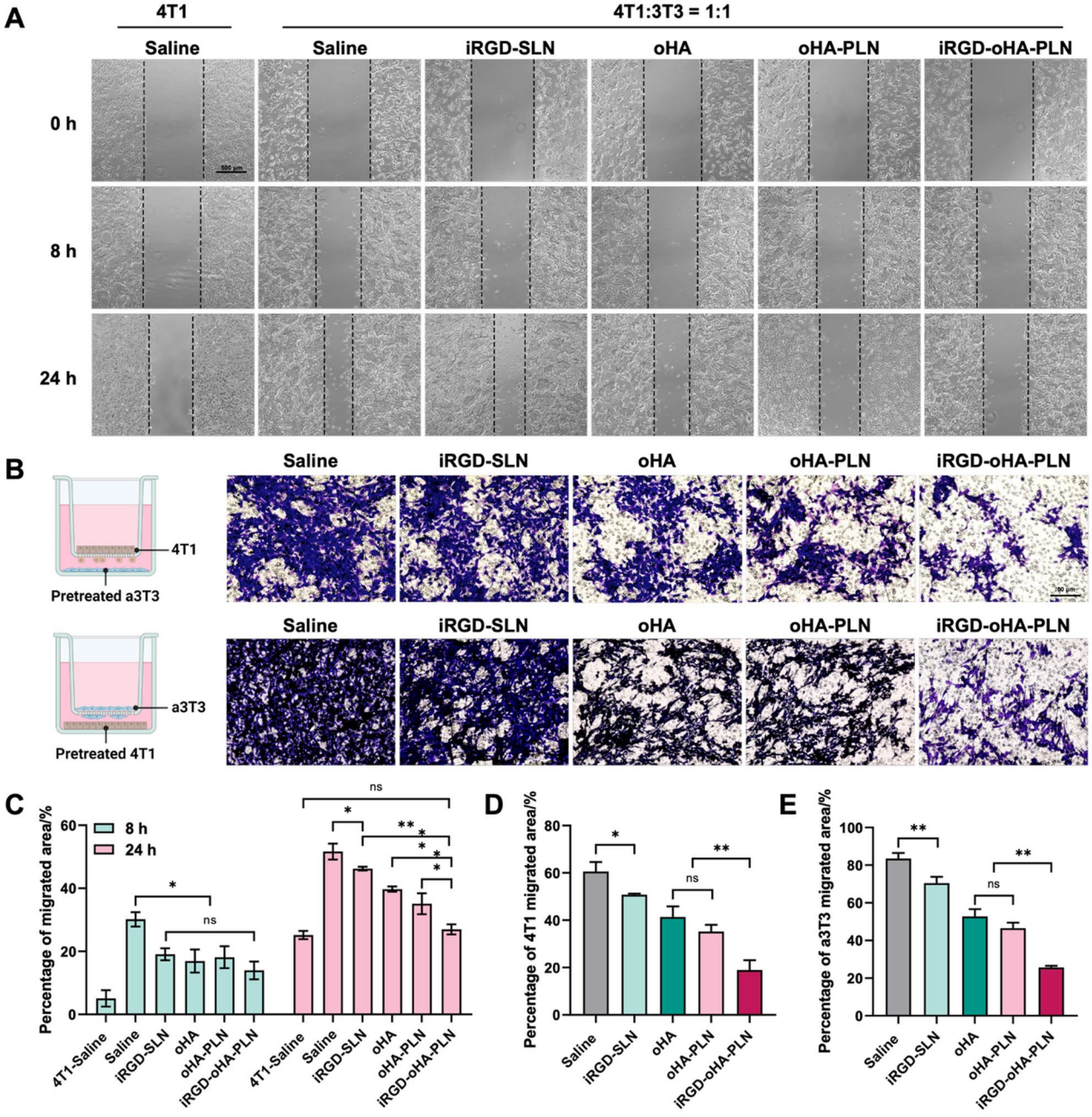

Fig. 3 iRGD-oHA-PLNs effectively suppressed the migration of both tumor cells and fibroblasts. (**A**) Brightfield images of wound-healing assay. 4T1-luc cells or 4T1-luc and 3T3 cell mixture (1:1) were scratched with 1 mL tips and treated with saline, iRGD-SLN, free oHA, oHA-PLN, and iRGD-oHA-PLN, at the oHA concertation of 10 μg/mL. The migration of cells was observed at 0 h, 8 h, and 24 h after treatment. Scale bar = 500 μm (**B**) Images of the transwell migration assay of 4T1 cells under the chemoattractant effect of a3T3 cells and a3T3 cells under the chemoattractant effect of 4T1-luc cells for 24 h. Cells in the lower chamber were pretreated with saline, free oHA, iRGD-SLN, free oHA, free oHA-PLN, and iRGD-oHA-PLN, at concentrations of oHA = 10 μg/mL for 24 h. Scale bar = 100 μm (**C**) Quantification of the recovery area at 8 and 24 h after scarification and treatment by the wound-healing assay ($n = 3$). (**D**) Quantification of 4T1-luc migrated area at 24 h after treatment by a transwell migration assay ($n = 3$). **(E)** Quantification of a3T3 migrated area at 24 h after treatment ($n = 3$). Data are presented as mean ± SD. ns: non-significant. *$p < 0.05$. **$p < 0.01$

> oHA > iRGD-SLN. Notably, treatment with iRGD-oHA-PLN seemed to counteract the CAF-mediated enhancement of cancer cell migration, while showing no significant difference in the migration area compared with 4T1 monoculture at 24 h (Fig. 3C). The impact of iRGD-SLN could be attributed to the disruption of integrin signaling by iRGD [33]. The binding of iRGD with integrins overexpressed on both TNBC cells and CAFs led to the internalization of integrins [34].

Transwell assays were conducted to further investigate paracrine interactions between cancer cells and CAFs. Pretreated 4T1 or a3T3 cells were placed in the lower chamber to assess their ability to recruit a3T3 or 4T1 cells in the upper chamber through the secretion of cytokines, chemokines, and chemoattractant factors. Migrated cells were visualized using crystal violet staining. Consistent with the wound healing results, both blank iRGD-SLN and oHA-PLN inhibited migration, while the iRGD-oHA-PLN showed the most pronounced inhibitory effect on both 4T1 and a3T3 cells (Fig. 3B, D, and E). Given that both cell types express integrins and CD44, it is plausible that iRGD and oHA influence their downstream signaling, thereby altering cytokine and chemokine levels in cancer cells and CAFs. Furthermore, oHA that was taken up by the pretreated and reseeded cells may be released and directly affect the cells in the upper chamber, regulating their motility [21]. In a related study to examine DOX-loaded formulations, cell migration was further inhibited by the combination of DOX + oHA, whether formulated as free drugs or nanoparticles, compared to oHA treatment alone (Figure S2 and S3) due to the cytotoxicity of DOX. Collectively, these findings suggest that iRGD-DOX-oHA-PLN impedes tumor progression by suppressing reciprocal migration of CAF and tumor cell, primarily mediated through CD44-HA interaction.

Regulation of TGF-β and the CXCL12/CXCR4 axis

To further explore the underlying mechanism by which iRGD-DOX-oHA-PLN inhibit cell migration, we investigated the modulation of cytokines and chemokines associated with CD44-HA downstream signaling pathway, with a particular focus on TGF-β and CXCL12/CXCR4 axis. TGF-β is abundantly produced by both CAFs and cancer cells, and plays a pivotal role in cancer proliferation, invasion, and immunosuppression [35]. To assess relative levels of cellular release, cell supernatants were collected from 4T1 and a3T3 cells pretreated for 24 h with different treatments and the TGF-β expression levels were measured. Intriguingly, iRGD-SLN alone reduced TGF-β secretion by 25% in 4T1 cells and 19% in a3T3 cells (Fig. 4A and B). This reduction corresponds with the findings from our anti-migration studies (Fig. 3), which are likely due to the disruption of integrin signaling [36]. Treatments with oHA markedly diminished TGF-β production, while iRGD-oHA-PLN treatment exhibited the strongest inhibitory effect with a 69% reduction in both cell types. This reduction is likely attributable to the inhibition of the Ras/MAPK signaling pathway [37, 38]. Additionally, TGF-β levels in mouse tumors measured three days post-single-dose treatments indicated that iRGD-DOX-PLN did not alter TGF-β levels, whereas the combination of DOX and oHA significantly lowered its production (Fig. 4C). Notably, iRGD-DOX-oHA-PLN demonstrated a superior effect on decreasing TGF-β level, with a reduction of 60% compared to saline control (Fig. 4C).

The emerging role of the CXCL12/CXCR4 signaling axis in breast cancer development has been recognized increasingly in recent years [39, 40]. Tumor cells expressing CXCR4 respond to CXCL12, promoting tumor cell proliferation and migration. Research has shown that oHA can disrupt CXCR4 signaling in liver cancer cells and human umbilical vein endothelial cells through interaction with CD44, in contrast to the signaling augmentation by native HA [51]. We therefore investigated whether oHA-containing formulations could alter the CXCL12/CXCR4 signaling between 4T1 and a3T3 cells. The results showed that CXCR4 expression in 4T1 cells was increased following treatment with a3T3 conditioned media (Fig. 4E and G), attributable to elevated native HA secreted by CAFs [41, 42]. Conversely, oHA treatment reduced CXCR4 expression in 4T1 cells (Fig. 4E). A similar trend was also observed in DOX and oHA combination treatment, where DOX alone did not alter CXCR4 levels, highlighting the role of oHA (Figure S4). Consistent with these in vitro findings, in vivo analysis further demonstrated that iRGD-DOX-oHA-PLN treatment significantly inhibited both CXCL12 secretion and CXCR4 expression in mouse tumors, as measured by ELISA and immunohistochemical (IHC) staining, respectively (Fig. 4D, F, and H).

Collectively, the above findings indicate that inhibiting CD44-HA downstream signaling pathways, particularly TGF-β and CXCL12/CXCR4, could significantly hinder tumor cell survival and migration, thereby suppressing metastasis of TNBC.

Regulation of ECM collagen production and orientation

Elevations in collagen levels in TNBC have been shown to drive pro-tumorigenic biology by enhancing ECM stiffness supporting tumor survival, proliferation, and EMT [43]. Collagen fiber scaffolds contribute to immune evasion by restricting cytotoxic T-cell infiltration and recruiting immunosuppressive cells, such as regulatory T cells and tumor-associated macrophages, through CXCR4/CXCL12 axis [44]. These processes collectively establish a tumor-permissive microenvironment, accelerating TNBC progression and metastasis [43, 45]. Among the various types of collagens, type I collagen is the most abundant form, has been extensively studied for its role in solid tumors. TGF-β has been identified as one of the key regulators of collagen secretion [46, 47]. Correlation analysis in TNBC patient samples revealed a strong positive relationship between the TGF-β encoding gene TGFB1 and the collagen-encoding genes COL1A1 and COL1A2, with Pearson correlation coefficients of 0.60

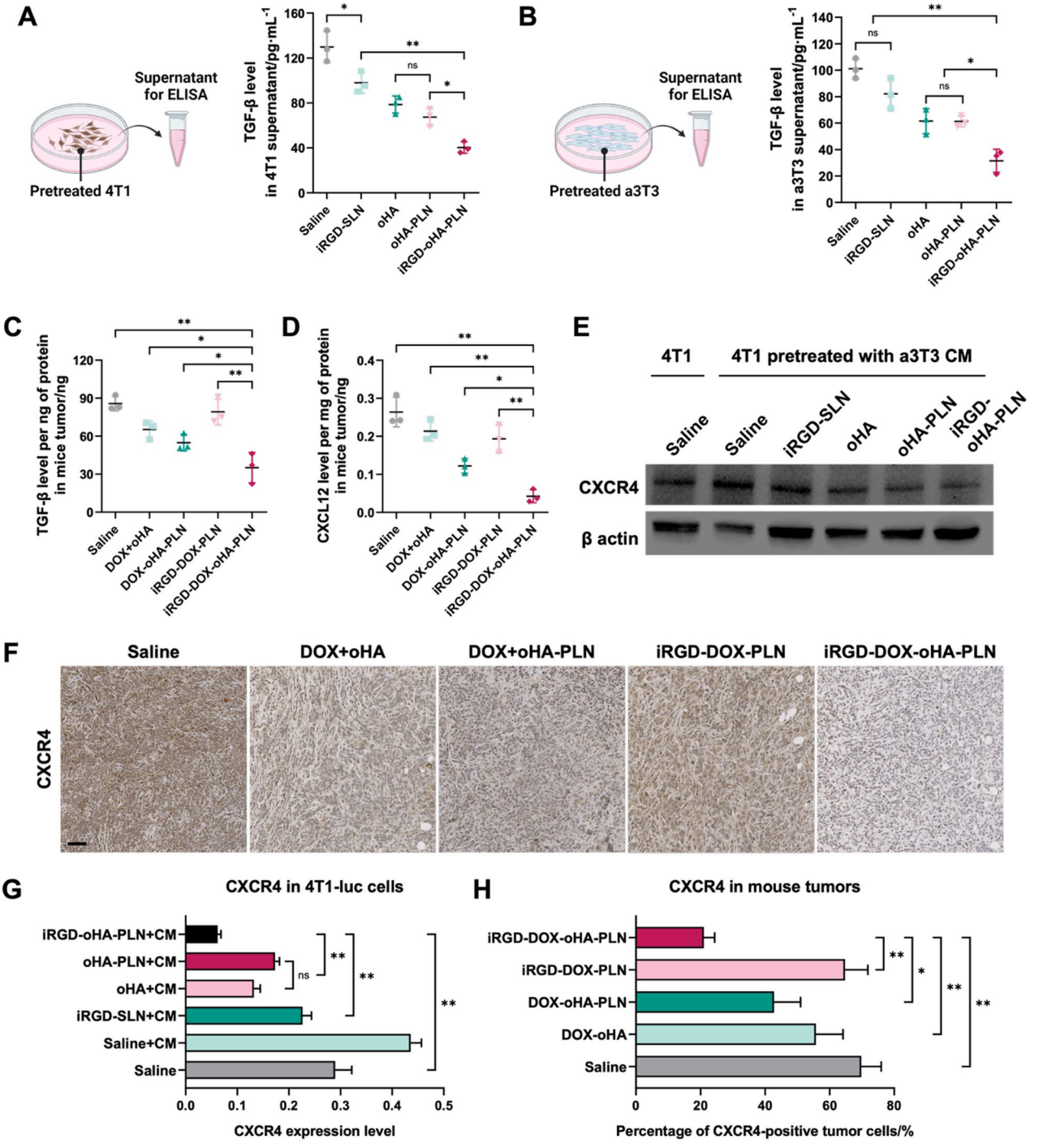

Fig. 4 iRGD-DOX-oHA-PLN attenuated paracrine communication between tumor cells and fibroblasts. TGF-β generated by (**A**) 4T1-luc cells and (**B**) a3T3 cells, measured by ELISA assay at 24 h post-treatments of saline, iRGD-SLN, free oHA, oHA-PLN, and iRGD-oHA-PLN at the concentration of oHA = 10 μg/mL. $n = 3$. (**C**) TGF-β and (**D**) CXCL12 in mice tumor tissues, measured by ELISA assay. Mice transplanted with orthotopic 4T1-luc tumors were treated with saline, free DOX-oHA, DOX-oHA-PLN, iRGD-DOX-PLN, and iRGD-DOX-oHA-PLN at the dose of DOX = 10 mg/kg. Tumors were harvested, homogenized, and analyzed 3 days after treatments. $n = 3$. (**E**) Western blot images of CXCR4 and β-actin in 4T1-luc cells, with or without the pretreatment of a3T3 conditioned media for 24 h. Cells were treated with saline, free oHA, free DOX, free DOX-oHA, iRGD-DOX-PLN, and iRGD-DOX-oHA-PLN at a DOX concentration of 0.5 μg/mL for 24 h. (**F**) Immunohistochemical staining images displaying CXCR4 expression in mouse 4T1-luc tumors 3 days after treatment. Scale bar = 100 μm (**G**) Fold changes of CXCR4 expression levels in 4T1-luc cells. (**H**) Quantitative analysis of the percentage of CXCR4-positive tumor cells. Protein expression levels were normalized to β-actin. $n = 3$ mice for each treatment. $n = 3$ sections for each mouse. Data are presented as mean ± SD. $^{*}p < 0.05$. $^{**}p < 0.01$

and 0.53, respectively (Figure S5). Additionally, a strong positive correlation was observed between CAF markers (FAP, ACTA2) and collagen-encoding genes (COL1A1, COL1A2) (Figure S5).

Building upon these findings, particularly the reduction of TGF-β secretion, we examined whether iRGD-DOX-oHA-PLN treatment affected type I collagen production [48]. Immunofluorescence results demonstrated a significant increase in type I collagen signal in a3T3, indicating greater collagen production compared to 3T3 cells (Fig. 5A). Treatments with iRGD-SLN and oHA-PLN appeared to reduce collagen production, with the iRGD-oHA-PLN demonstrating the most pronounced effects. This reduction in collagen content could block the invasion pathways of tumor cells and influence pro-invasive signals by reducing ECM stiffness.

To explore the role of collagen in structural support of cancer cell invasion, an invasion assay was conducted using a 3D spheroid of 3T3 and 4T1 cell co-culture. Typically, type I collagen from rat tails is commonly utilized in 3D invasion studies; however, to avoid confounding factors related to external collagen sources, growth factor-reduced Matrigel was chosen to encapsulate the co-culture spheroids [49, 50]. Considering the highly epithelial characteristics of 4T1 cells and the absence of collagen in the matrix, a high ratio of 3T3 cells (10:1) was employed. At 4 days after treatment, the representative images showed that spheroids in the saline control group exhibited a markedly invasive morphology characterized by an extensive projection area (Fig. 5B). In comparison, treatment with iRGD-SLN and oHA-containing formulations significantly reduced cell invasion, suggesting a combined effect of collagen and cytokine reduction.

To assess the presence of CAFs and total collagen in mouse tumors, we utilized female BALB/c mice with orthotopic 4T1-luc TNBC tumors. It is important to note that the stroma ratio within tumors can vary over time. Prior studies have revealed that the stroma of 4T1 orthotopic tumors becomes more enriched following at least two weeks of growth [51]. To ensure a robust analysis, tumors were treated and subsequently harvested approximately three weeks post-inoculation. Quantitative evaluations of the CAF marker, α-SMA, revealed a minimal impact from administering free DOX + oHA combination (Fig. 5C and D). However, DOX-oHA-PLN administration significantly reduced α-SMA and total collagen levels by 21% and 41%, respectively, compared to saline control. The iRGD-DOX-oHA-PLN formulation further reduced these levels by 47% and 62%, respectively. In contrast, treatment with iRGD-DOX-PLN led to a 30% reduction of CAFs relative to saline, though its effect on collagen production was less pronounced with only a 27% reduction. These results suggest that the decrease in CAFs is predominantly driven by the enhanced tumor targeting and cytotoxic effects of DOX delivered using nanoparticles. Furthermore, the co-delivery of oHA and DOX can synergistically improve the treatments effectiveness in reducing collagen content beyond merely reducing CAF population.

In addition to collagen density, the orientation of collagen fibers, particularly those surrounding tumors, serves as a crucial prognostic indicator of breast cancer patients [52, 53]. Several TACS have been defined, each representing a distinct pattern of collagen architectures [53]. Notably, at the periphery of tumors treated with saline (control group), we detected a pronounced presence of TACS5 characterized by collagen fibers that are straightened and aligned perpendicularly towards the tumor periphery without a clear boundary (Fig. 5C) [53]. This pattern indicates the disruption of the basement membrane and favors unidirectional migration and invasion of tumor cells. The TACS6 configuration, characterized by disordered collagen fibers that promote multidirectional tumor cell migration, was also noted in the group administered with free DOX + oHA. It is important to highlight that both TACS5 and TACS6 are associated with an adverse prognosis in patients. In contrast, TACS7, a pattern linked to a more favorable prognosis, was more commonly observed in the tumors after treatment with DOX-oHA-PLN, iRGD-DOX-PLN, or iRGD-DOX-oHA-PLN, where collagen fibers aligned parallelly to the tumor margin, forming a distinct tumor boundary. Overall, these findings suggest that the iRGD-DOX-oHA-PLN treatment potentially impacts tumor cell mobility and invasion pathways by altering the structure of the ECM.

Regulation of EMT and MMP-9

The ECM is one of the key regulators of EMT, particularly through its protein component. For example, collagen promotes EMT by disrupting epithelial cell polarity, decreasing cell-cell adhesion, and increasing cell motility and invasiveness [54]. EMT is widely recognized as a pivotal biological process in cancer progression, facilitating tumor metastasis by enhancing cell migration and invading surrounding tissues [51]. In addition, ECM-driven upregulation of MMPs, particularly MMP-9, contributes to cancer invasion and metastasis by promoting EMT [55, 56].

The above results demonstrated that iRGD-DOX-oHA-TPN effectively regulates ECM by reducing CAFs and collagen, prompting us to further investigate its effect on EMT and MMP-9. The expression levels of key EMT markers (E-cadherin, N-cadherin) and MMP-9 in both 4T1 and a3T3 cells were evaluated by confocal microscopy and western blotting. The results demonstrated that DOX treatment alone did not alter E-cadherin and N-cadherin expression levels (Figure S6). By contrast, treatment with oHA significantly increased E-cadherin

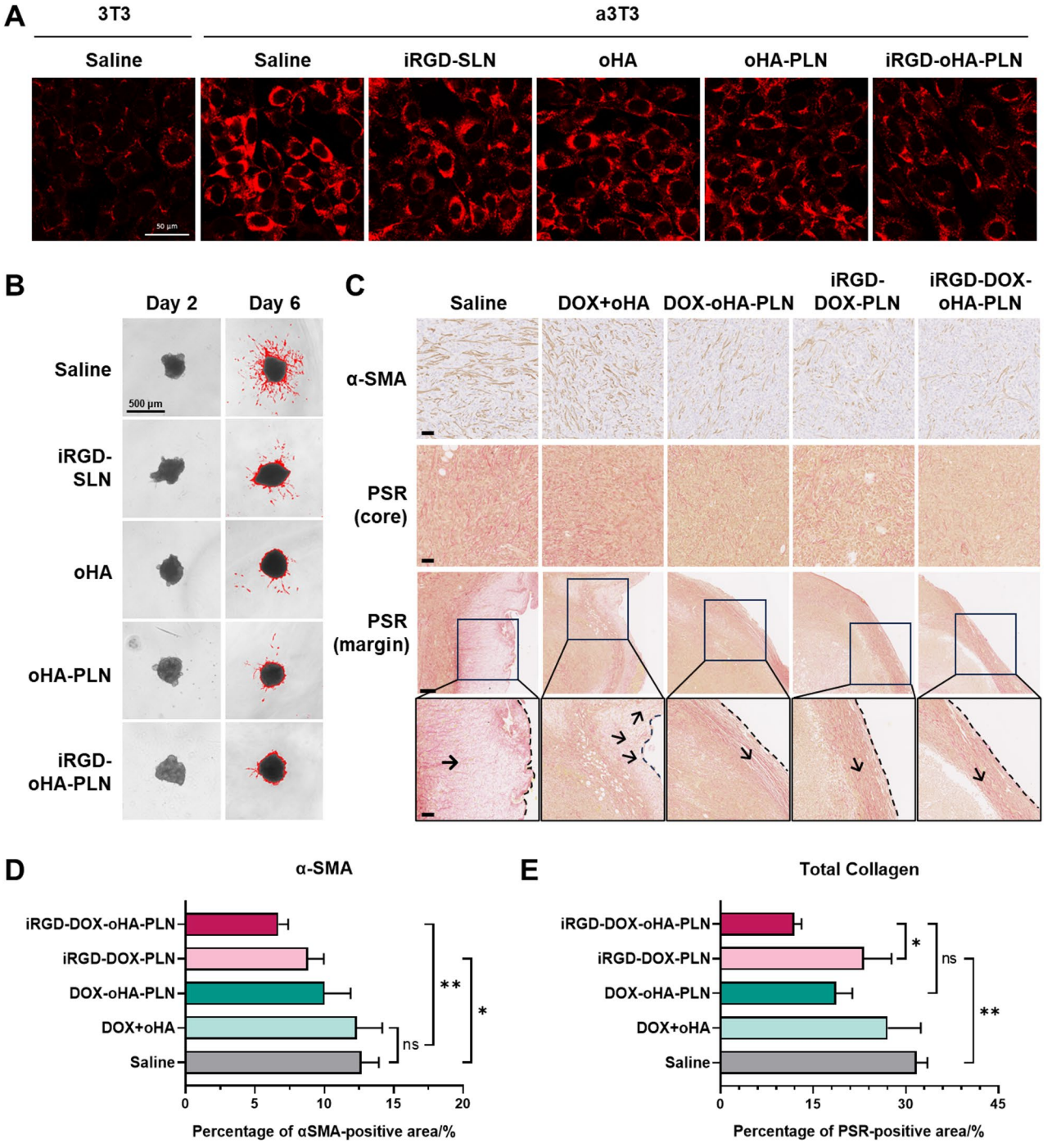

Fig. 5 iRGD-DOX-oHA-PLN depleted CAFs and reduced collagen production. (**A**) Confocal imaging examining collagen I expression in 3T3 or a3T3 cells. a3T3 cells were treated with saline, iRGD-SLN, free oHA, oHA-PLN, and iRGD-oHA-PLN at the oHA concentration of 10 μg/mL for 24 h. (**B**) Invasion assay conducted on co-cultures of 3T3 and 4T1-luc cells (10:1) in Matrigel. On day 2, spheroids generated in a round-bottom 96-well plate were embedded in Matrigel and treated with saline, iRGD-SLN, oHA, oHA-PLN, and iRGD-oHA-PLN, all at an equivalent oHA concentration of 10 μg/mL for 4 days. Brightfield images were taken on days 2 and 6. Invasion fronts were highlighted by color thresholding in ImageJ. (**C**) Immunohistochemical images examining α-SMA expression, picrosirius red (PR) staining indicating total collagen content, and PSR staining at tumor margins, in mouse 4T1-luc tumors 3 days after treatment. Dashed lines denote the tumor margin. Arrows illustrate the direction of collagen fibers. Scale bar = 50 μm for α-SMA and PSR (core). Scale bar = 250 μm for PSR (margin). Scale bar = 100 μm for enlarged PSR (margin). (**D**) Quantitative examination of the percentage of αSMA-positive area. (**E**) Quantitative analysis of the percentage of PSR-positive area. For in vivo studies, $n = 3$ mice for each treatment. For IHC staining, $n = 3$ sections for each mouse. Data are presented as mean ± SD. *$p < 0.05$. **$p < 0.01$; ns: non-significant

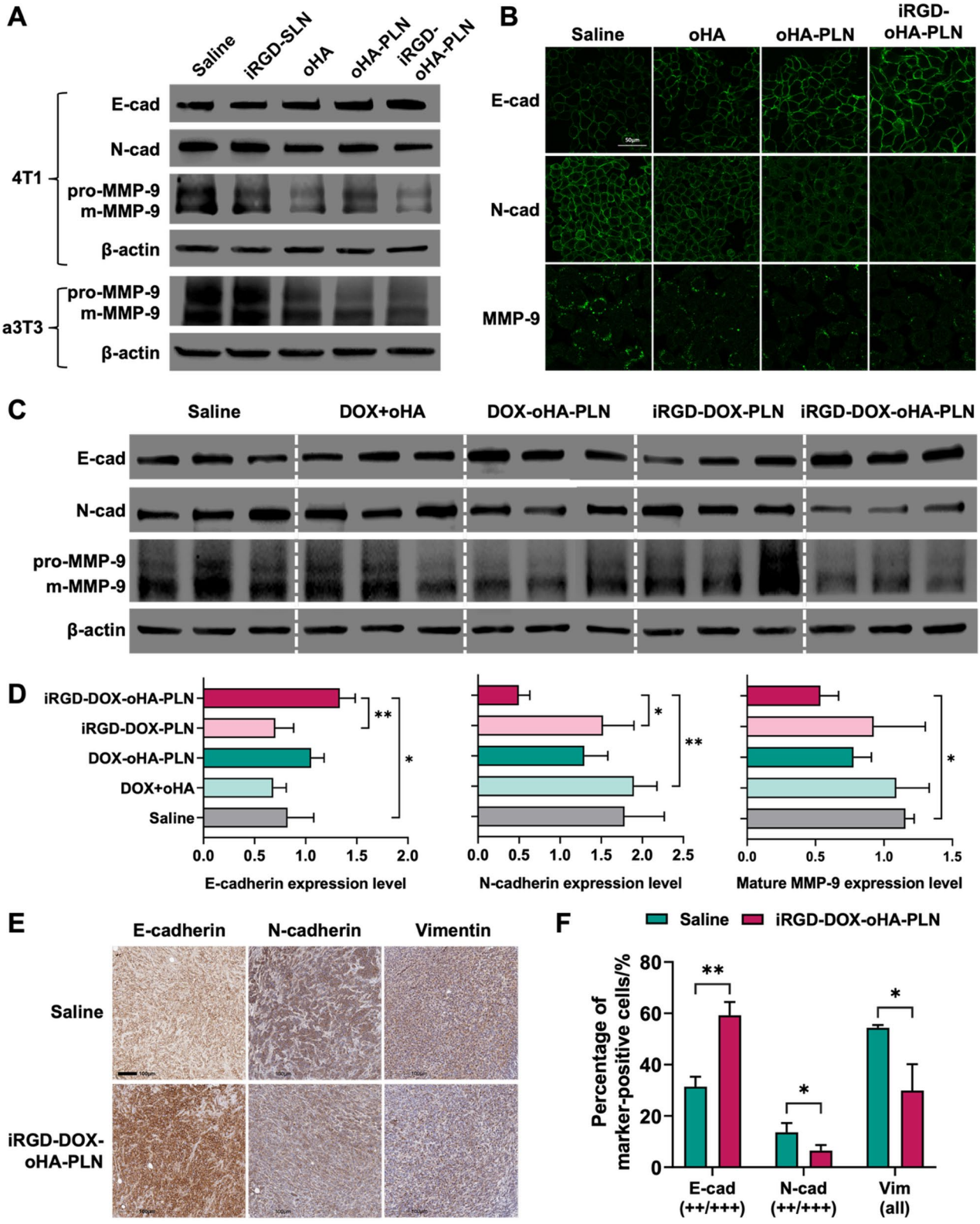

Fig. 6 (See legend on next page.)

(See figure on previous page.)

Fig. 6 iRGD-DOX-oHA-PLN suppresses EMT and reduces MMP-9 expression. (**A**) Western blot of E-cadherin, N-cadherin, MMP-9, and β-actin in 4T1-luc cells or a3T3 cells following treatment with saline, iRGD-SLN, free oHA, oHA-PLN, and iRGD-oHA-PLN at an equivalent oHA concentration of 10 μg/mL for 24 h. Pro-MMP-9 represents the parent (inactive) form of MMP-9; m-MMP-9 represents the mature (active) MMP-9 isoform. (**B**) Confocal imaging of E-cadherin, N-cadherin, and MMP-9 expression in 4T1-luc cells following treatment with saline, free oHA, oHA-PLN or iRGD-oHA-PLN at an equivalent oHA concentration of 10 μg/mL for 24 h. Scale bar = 50 μm. (**C**) Western blot of E-cadherin, N-cadherin, MMP-9, and β-actin in mouse tumors. Mice with orthotopic 4T1-luc tumors were treated with saline, free DOX-oHA, DOX-oHA-PLN, iRGD-DOX-PLN, and iRGD-DOX-oHA-PLN at the dose of DOX = 10 mg/kg. Tumors were harvested, homogenized, and analyzed 3 days after treatments. (**D**) Fold changes of E-cadherin, N-cadherin, and MMP-9 expression in mouse tumors. Protein expression levels were normalized to β-actin. $n = 3$. (**E**) Representative images of immunohistochemical staining of E-cadherin, N-cadherin, and vimentin in tumor sections. Mice with 4T1 orthotopic breast tumors were treated with saline and iRGD-DOX-oHA-PLN ([DOX] = 10 mg/kg) for 3 days before tumor resection. Scale bar = 100 μm. (**F**) Percentages of moderate (++) and strong (+++) E-cadherin-positive cells, moderate (++) and strong (+++) N-cadherin-positive cells, and all vimentin-positive cells. $n = 3$ mice for each treatment. $n = 3$ sections for each mouse. Data are presented as mean ± SD. $^{*}p < 0.05$. $^{**}p < 0.01$

expression while decreasing N-cadherin and MMP-9 levels, differing markedly from results observed in either saline or blank iRGD-SLN treatment groups (Fig. 6A, B). Of those examined, the iRGD-oHA-PLN treatment group exhibited the most pronounced effect on inhibiting EMT by enabling higher cellular uptake. Consistently, western blot analysis of tumor samples further revealed that free DOX + oHA and iRGD-DOX-PLN treatments were ineffective in modulating EMT and MMP-9 maturation (Fig. 6C and D). DOX-oHA-PLN treatment increased E-cadherin by 28%, decreased N-cadherin and MMP-9 by 27% and 33%, respectively compared to saline. The iRGD-DOX-oHA-PLN treatment significantly impeded the EMT, with a more pronounced effect on these markers, increasing E-cadherin by 62%, decreasing N-cadherin and MMP-9 levels by 72% and 54%, respectively. IHC analysis of tissue sections revealed consistent findings regarding the modulation of E-cadherin and N-cadherin (Fig. 6E). The EMT inhibition may arise from regulating tumor cells by suppressing the CD44-HA downstream signalling pathways, such as TGF-β, PI3K/Akt, and MAPK/ERK signaling pathways [57, 58]. Remarkably, evaluation of vimentin, a marker indicative of mesenchymal cancer cells and fibroblasts, demonstrated a substantial (46%) reduction following iRGD-DOX-oHA-PLN treatment (Fig. 6F), furtherly demonstrating the dual effect of iRGD-DOX-oHA-PLN on inhibiting EMT and reducing CAFs. These findings highlight the superior tumor accumulation of the iRGD-DOX-oHA-PLN formulation and demonstrate its efficacy on suppressing tumor invasion by inhibiting EMT and reducing MMP-9, suggesting its potential to mitigate cancer metastasis.

Conclusion and discussion

In this study, we developed a multitargeted nanoparticle (iRGD-DOX-oHA-PLN) designed to simultaneously disrupt tumor cells and CAFs, two key drivers of TNBC progression. While CAF enrichment and collagen deposition are known features of TNBC, our data further establish their clinical relevance by linking elevated CAF and CAF-associated type I collagen with poor patient outcomes, reinforcing CAFs as a critical therapeutic target.

Mechanistically, the therapeutic effect of iRGD-DOX-oHA-PLN arises from a coordinated three-level intervention: enhanced delivery, stromal-tumor signaling disruption, and ECM remodeling. First, iRGD functionalization enables preferential uptake in CAFs through integrin αvβ3/β5 overexpression, resulting in higher intracellular delivery of DOX and oHA compared to normal fibroblasts. This selective targeting is essential, as CAFs are otherwise difficult to eliminate and contribute disproportionately to tumor progression.

Second, at the signaling level, oHA blocks CD44-HA interactions, leading to suppression of downstream CXCL12/CXCR4 and TGF-β pathways. These pathways form a bidirectional signaling loop between CAFs and TNBC cells that amplifies tumor invasion, metastasis, and immune evasion [31, 59]. By disrupting this loop, iRGD-DOX-oHA-PLN attenuates CAF-tumor crosstalk at its source [39, 40, 60]. Importantly, this effect extends beyond direct cytotoxicity: inhibition of CXCL12/CXCR4 and TGF-β reduces recruitment and polarization of immunosuppressive cells (e.g., M2 tumor-associated macrophage, myeloid-derived suppressor cells and regulatory T cells) while restoring dendritic cell and cytotoxic T cell activity, thereby shifting the tumor microenvironment toward an anti-tumor immune state [26, 61–64].

Third, at the structural level, iRGD-DOX-oHA-PLN remodels the ECM by reducing collagen production and altering fiber organization. The decrease in collagen density, together with the transition from radially aligned to tumor-encapsulating collagen fibers, suggests reduced ECM stiffness and impaired invasion pathways. Given that ECM stiffness is a key regulator of EMT, this remodeling provides a mechanistic link to the observed increase in E-cadherin and decrease in N-cadherin and MMP-9 expression [65, 66]. Thus, ECM normalization represents a critical downstream consequence of CAF inhibition and contributes to reduced metastatic potential.

The novelty of this study lies in integrating these mechanisms into a single platform that simultaneously targets CAFs, tumor cells, and the ECM-immune axis. While previous approaches have focused on either CAF depletion, CD44 inhibition, or nanoparticle-mediated drug

delivery alone, our system uniquely combines: (i) iRGD-mediated CAF-selective delivery, (ii) oHA-driven blockade of CD44-dependent stromal-tumor signaling, and (iii) concurrent chemotherapeutic and TME-modulating effects. This multi-layered strategy enables not only direct tumor cell killing but also reprogramming of the tumor microenvironment, addressing key limitations of conventional therapies that fail to overcome stromal barriers and immunosuppression.

Collectively, our findings support a model in which iRGD-DOX-oHA-PLN suppresses TNBC progression by disrupting CAF-tumor feedback signaling, normalizing ECM architecture, and alleviating immunosuppression. This coordinated targeting of cellular, molecular, and biophysical components of the tumor microenvironment highlights a promising therapeutic paradigm for TNBC and other desmoplastic cancers.

Future direction

Based on our current findings about TME regulation by iRGD-DOX-oHA-PLN, primarily CAFs and collagen, future studies should focus on further elucidating the mechanisms underlying TME remodeling and enhancing the translational potential of iRGD-DOX-oHA-PLN. Given the observed reduction in collagen deposition and reorganization of ECM architecture, quantitative assessment of tumor stiffness and its correlation with drug penetration and metastatic suppression would provide valuable mechanistic insight. Additionally, the heterogeneity of CAF populations should be explored to identify which subsets are most responsive to treatment. From a therapeutic perspective, combining iRGD-DOX-oHA-PLN with immune checkpoint blockade or other pathway-specific inhibitors, such as CXCR4 or TGF-β antagonists, may further enhance anti-tumor efficacy by overcoming residual immunosuppression. Furthermore, systematic evaluation of pharmacokinetics, biosafety, and large-scale formulation feasibility will be essential to facilitate clinical translation, while the modular design of this nanoparticle system also offers opportunities for adaptation to other stromal-rich malignancies.

Abbreviations

TNBC	Triple-negative breast cancer
ER	Estrogen receptor
PR	Progesterone receptor
HER2	Human epidermal growth factor receptor 2
CAFs	Cancer-associated fibroblasts
EMT	Epithelial-to-mesenchymal
TME	Tumor microenvironment
α-SMA	α-smooth muscle actin
FAP	Fibroblast activation protein
TGF-β	Transforming growth factor-β
IL-6	Interleukin-6
CXCL12	CXC-chemokine ligand 12
CXCR4	C-X-C chemokine receptor type 4
ECM	Extracellular matrix
HA	Hyaluronan
oHA	Oligomeric HA
CD44	Cluster of Differentiation 44
RHAMM	Receptor for Hyaluronic Acid Mediated Motility
MAPK/ERK	Mitogen-activated protein kinase/extracellular-signal-regulated kinase
PI3K	Phosphoinositide 3-kinase
MMPs	Matrix metalloproteinases
DOX	Doxorubicin
iRGD	Internalizing RGD
NRP-1	Neuropilin-1
TCGA	The Cancer Genome Atlas
IHC	Immunohistochemical
TACS	Tumor-associated collagen signatures

Supplementary Information

The online version contains supplementary material available at https://doi.org/10.1186/s12951-026-04526-8.

Supplementary Material 1.

Supplementary Material 2.

Supplementary Material 3.

Acknowledgements

The authors thank the National Science and Engineering Research Council (NSERC) of Canada for the Equipment Grants and the Canadian Institutes of Health Research (CIHR) for the project funding to X.Y. Wu. The Graduate Department of Pharmaceutical Sciences, University of Toronto, for student support. The Chinese Scholarship Council for the scholarship to P. Zhi and the King Abdulaziz City for Science and Technology (KACST) scholarship to I. Alradwan. The technical contribution in the breast tumor sample processing and immunohistochemistry staining from Dr. Andrew J. Elia and Farseema Delgosha of the Campbell Family Institute for Breast Cancer Research, Ontario Cancer Institute, and University Health Network. Dr. Andrew J. Elia, Staff Scientist, Centre for Integrative Immune Analysis, CIIA Histology Core, Princess Margaret Cancer Centre, PMH/University Health Network.

Author contributions

L.W. and P.Z. contributed equally to this work; P.Z. and X.Y.W. performed conceptualization and design of the project; P.Z. and L.W. conducted the majority of the experiments and analyzed the data; I.A. provided technical expertise and contributed to data analysis; P.Z., L.W., I.A., C.H., A.Z.A., and X.Y.W. contributed to writing – original draft and assisted with experimental design, providing critical insights during data interpretation; H.G. and J.T.H. contributed to the literature review and manuscript revision; X.Y.W. supervised the project, provided funding and resources, and finalized the manuscript for submission. All authors contributed to the writing of the manuscript, reviewed and approved the final version.

Funding

This work was supported in part by the Canadian Breast Cancer and Foundation-Ontario Region, the Canadian Institutes of Health Research (CIHR) Project Grant (#PJT-168872), the Natural Sciences & Engineering Research Council of Canada (NSERC) Discovery Grant (RGPIN-2025-07078), and Equipment Grant (EQPEQ 440689-13).

Data availability

The data is freely available upon request from the Corresponding Author:

Xiao Yu Wu* - Advanced Pharmaceutics and Drug Delivery Laboratory, Leslie Dan Faculty of Pharmacy, University of Toronto, 144 College Street, Toronto, Ontario, Canada, M5S 3M2; E-mail: sxy.wu@utoronto.ca; ORCID: Xiao Yu Wu (0000-0002-5333-8115).

Declarations

Competing interests

The authors declare no competing interests.

Author details
[1]Advanced Pharmaceutics and Drug Delivery Laboratory, Leslie Dan Faculty of Pharmacy, University of Toronto, Toronto M5S3M2, ON, Canada
[2]Advanced Diagnostics and Therapeutics Institute, King Abdulaziz City for Science and Technology (KACST), Riyadh, Saudi Arabia
[3]Departments of Medical Biophysics and Radiation Oncology, University of Toronto, 610 University Ave, Toronto M5G2M9, ON, Canada
[4]Department of Medical Oncology and Hematology, Princess Margaret Cancer Centre/University Health Network, 700 University Ave, Toronto M5G2M9, ON, Canada

Received: 18 December 2025 / Accepted: 27 April 2026
Published online: 18 May 2026

References

1. Won K-A, Spruck C. Triple–negative breast cancer therapy: Current and future perspectives (Review). Int J Oncol. 2020;57:1245–61. https://doi.org/10.3892/ijo.2020.5135.
2. Garrido-Castro AC, Lin NU, Polyak K. Insights into Molecular Classifications of Triple-Negative Breast Cancer: Improving Patient Selection for Treatment. Cancer Discov. 2019;9:176–98. https://doi.org/10.1158/2159-8290.CD-18-1177.
3. Dent R, Trudeau M, Pritchard KI, Hanna WM, Kahn HK, Sawka CA, et al. Triple-negative breast cancer: clinical features and patterns of recurrence. Clin Cancer Res. 2007;13:4429–34. https://doi.org/10.1158/1078-0432.CCR-06-3045.
4. Early Breast Cancer Trialists' Collaborative Group (EBCTCG), Peto R, Davies C, Godwin J, Gray R, Pan HC, et al. Comparisons between different polychemotherapy regimens for early breast cancer: meta-analyses of long-term outcome among 100,000 women in 123 randomised trials. Lancet. 2012;379:432–44. https://doi.org/10.1016/S0140-6736(11)61625-5.
5. Birbrair A, editor. Tumor Microenvironment: Extracellular Matrix Components – Part A [Internet]. Cham: Springer International Publishing; 2020. https://doi.org/10.1007/978-3-030-40146-7. [cited 2025 Jan 16].
6. Erez N, Truitt M, Olson P, Arron ST, Hanahan D. Cancer-Associated Fibroblasts Are Activated in Incipient Neoplasia to Orchestrate Tumor-Promoting Inflammation in an NF-kappaB-Dependent Manner. Cancer Cell. 2010;17:135–47. https://doi.org/10.1016/j.ccr.2009.12.041.
7. Löhr M, Schmidt C, Ringel J, Kluth M, Müller P, Nizze H, et al. Transforming growth factor-beta1 induces desmoplasia in an experimental model of human pancreatic carcinoma. Cancer Res. 2001;61:550–5.
8. Aoyagi Y, Oda T, Kinoshita T, Nakahashi C, Hasebe T, Ohkohchi N, et al. Overexpression of TGF-beta by infiltrated granulocytes correlates with the expression of collagen mRNA in pancreatic cancer. Br J Cancer. 2004;91:1316–26. https://doi.org/10.1038/sj.bjc.6602141.
9. Yang D, Liu J, Qian H, Zhuang Q. Cancer-associated fibroblasts: from basic science to anticancer therapy. Exp Mol Med [Internet] Nat Publishing Group. 2023;55:1322–32. https://doi.org/10.1038/s12276-023-01013-0. [cited 2025 Oct 27];.
10. Chen X, Song E. Turning foes to friends: targeting cancer-associated fibroblasts. Nat Rev Drug Discov Nat Publishing Group. 2019;18:99–115. https://doi.org/10.1038/s41573-018-0004-1.
11. Liu H, Yang Z, Lu W, Chen Z, Chen L, Han S, et al. Chemokines and chemokine receptors: A new strategy for breast cancer therapy. Cancer Med. 2020;9:3786–99. https://doi.org/10.1002/cam4.3014.
12. Chen Y, McAndrews KM, Kalluri R. Clinical and therapeutic relevance of cancer-associated fibroblasts. Nat Rev Clin Oncol Nat Publishing Group. 2021;18:792–804. https://doi.org/10.1038/s41571-021-00546-5.
13. Zhang H, Yue X, Chen Z, Liu C, Wu W, Zhang N, et al. Define cancer-associated fibroblasts (CAFs) in the tumor microenvironment: new opportunities in cancer immunotherapy and advances in clinical trials. Mol Cancer. 2023;22:159. https://doi.org/10.1186/s12943-023-01860-5.
14. Liu T, Han C, Wang S, Fang P, Ma Z, Xu L, et al. Cancer-associated fibroblasts: an emerging target of anti-cancer immunotherapy. J Hematol Oncol. 2019;12:86. https://doi.org/10.1186/s13045-019-0770-1.
15. Tomasek JJ, Gabbiani G, Hinz B, Chaponnier C, Brown RA. Myofibroblasts and mechano-regulation of connective tissue remodelling. Nat Rev Mol Cell Biol Nat Publishing Group. 2002;3:349–63. https://doi.org/10.1038/nrm809.
16. Liu T, Zhou L, Li D, Andl T, Zhang Y. Cancer-Associated Fibroblasts Build and Secure the Tumor Microenvironment. Front Cell Dev Biol. 2019;7:60. https://doi.org/10.3389/fcell.2019.00060.
17. Brett EA, Sauter MA, Machens H-G, Duscher D. Tumor-associated collagen signatures: pushing tumor boundaries. Cancer Metab. 2020;8:14. https://doi.org/10.1186/s40170-020-00221-w.
18. Shi R, Zhang Z, Zhu A, Xiong X, Zhang J, Xu J, et al. Targeting type I collagen for cancer treatment. Int J Cancer. 2022;151:665–83. https://doi.org/10.1002/ijc.33985.
19. Bayarmagnai B, Perrin L, Esmaeili Pourfarhangi K, Graña X, Tüzel E, Gligorijevic B. Invadopodia-mediated ECM degradation is enhanced in the G1 phase of the cell cycle. J Cell Sci. 2019;132:jcs227116. https://doi.org/10.1242/jcs.227116.
20. Kinugasa Y, Matsui T, Takakura N. CD44 expressed on cancer-associated fibroblasts is a functional molecule supporting the stemness and drug resistance of malignant cancer cells in the tumor microenvironment. Stem Cells. 2014;32:145–56. https://doi.org/10.1002/stem.1556.
21. Zhang T, Fu C, Alradwan I, Yen T, Lip H, Cai P et al. Targeting Signaling Pathways of Hyaluronic Acid and Integrin Receptors by Synergistic Combination Nanocomposites Inhibits Systemic Metastases and Primary Triple Negative Breast Cancer. Advanced Therapeutics [Internet]. 2021 [cited 2024 July 12];4:2100022. https://doi.org/10.1002/adtp.202100022
22. Toole BP. Hyaluronan-CD44 Interactions in Cancer: Paradoxes and Possibilities. Clin Cancer Res. 2009;15:7462–8. https://doi.org/10.1158/1078-0432.CCR-09-0479.
23. Cyphert JM, Trempus CS, Garantziotis S. Size Matters: Molecular Weight Specificity of Hyaluronan Effects in Cell Biology. Int J Cell Biol. 2015;2015:563818. https://doi.org/10.1155/2015/563818.
24. Wong HL, Rauth AM, Bendayan R, Manias JL, Ramaswamy M, Liu Z, et al. A New Polymer–Lipid Hybrid Nanoparticle System Increases Cytotoxicity of Doxorubicin Against Multidrug-Resistant Human Breast Cancer Cells. Pharm Res. 2006;23:1574–85. https://doi.org/10.1007/s11095-006-0282-x.
25. Shan D, Li J, Cai P, Prasad P, Liu F, Rauth AM, et al. RGD-conjugated solid lipid nanoparticles inhibit adhesion and invasion of αvβ3 integrin-overexpressing breast cancer cells. Drug Deliv Transl Res. 2015;5:15–26. https://doi.org/10.1007/s13346-014-0210-2.
26. Alradwan I, Zhi P, Zetrini AE, Wang L, He C, Rezaeifarimani M, et al. Empowering chemotherapy-induced antitumor immunity by multi-targeted synergistic combination nanomedicine for triple-negative breast cancer. Mater Today Bio. 2025;35:102445. https://doi.org/10.1016/j.mtbio.2025.102445.
27. Zhang T, Fu C, Alradwan I, Yen T, Lip H, Cai P, et al. Targeting Signaling Pathways of Hyaluronic Acid and Integrin Receptors by Synergistic Combination Nanocomposites Inhibits Systemic Metastases and Primary Triple Negative Breast Cancer. Adv Ther. 2021;4:2100022. https://doi.org/10.1002/adtp.202100022.
28. Alradwan I, Zhi P, Zhang T, Lip H, Zetrini A, He C, et al. Nanoparticulate drug combination inhibits DNA damage repair and PD-L1 expression in BRCA-mutant and wild type triple-negative breast cancer. J Controlled Release. 2025;377:661–74. https://doi.org/10.1016/j.jconrel.2024.11.061.
29. Vangangelt KMH, Green AR, Heemskerk IMF, Cohen D, van Pelt GW, Sobral-Leite M, et al. The prognostic value of the tumor-stroma ratio is most discriminative in patients with grade III or triple-negative breast cancer. Int J Cancer. 2020;146:2296–304. https://doi.org/10.1002/ijc.32857.
30. Zakhartseva LM, Yanovytska MA, PROGNOSTIC VALUE OF TUMOR, STROMA RATIO IN TRIPLE NEGATIVE BREAST CANCER. Wiad Lek. 2021;74:565–71.
31. Sahai E, Astsaturov I, Cukierman E, DeNardo DG, Egeblad M, Evans RM, et al. A framework for advancing our understanding of cancer-associated fibroblasts. Nat Rev Cancer Nat Publishing Group. 2020;20:174–86. https://doi.org/10.1038/s41568-019-0238-1.
32. Affo S, Nair A, Brundu F, Ravichandra A, Bhattacharjee S, Matsuda M, et al. Promotion of cholangiocarcinoma growth by diverse cancer-associated fibroblast subpopulations. Cancer Cell Elsevier. 2021;39:866–e88211. https://doi.org/10.1016/j.ccell.2021.03.012.
33. Hood JD, Cheresh DA. Role of integrins in cell invasion and migration. Nat Rev Cancer Nat Publishing Group. 2002;2:91–100. https://doi.org/10.1038/nrc727.
34. Ludwig BS, Kessler H, Kossatz S, Reuning U, Ludwig BS, Kessler H et al. RGD-Binding Integrins Revisited: How Recently Discovered Functions and Novel Synthetic Ligands (Re-)Shape an Ever-Evolving Field. Cancers [Internet]. publisher; 2021 [cited 2025 Dec 15];13. https://doi.org/10.3390/cancers13071711
35. Derynck R, Akhurst RJ, Balmain A. TGF-beta signaling in tumor suppression and cancer progression. Nat Genet. 2001;29:117–29. https://doi.org/10.1038/ng1001-117.

36. Li S, Sampson C, Liu C, Piao H, Liu H-X. Integrin signaling in cancer: bidirectional mechanisms and therapeutic opportunities. Cell Communication Signal. 2023;21:266. https://doi.org/10.1186/s12964-023-01264-4.
37. Yue J, Mulder KM. Requirement of Ras/MAPK pathway activation by transforming growth factor beta for transforming growth factor beta 1 production in a Smad-dependent pathway. J Biol Chem. 2000;275:30765–73. https://doi.org/10.1074/jbc.M000039200.
38. Gui T, Sun Y, Shimokado A, Muragaki Y. The Roles of Mitogen-Activated Protein Kinase Pathways in TGF-β-Induced Epithelial-Mesenchymal Transition. J Signal Transduct. 2012;2012:289243. https://doi.org/10.1155/2012/289243.
39. Zielińska KA, Katanaev VL. The Signaling Duo CXCL12 and CXCR4: Chemokine Fuel for Breast Cancer Tumorigenesis. Cancers (Basel). 2020;12:3071. https://doi.org/10.3390/cancers12103071.
40. Gil M, Seshadri M, Komorowski MP, Abrams SI, Kozbor D. Targeting CXCL12/CXCR4 signaling with oncolytic virotherapy disrupts tumor vasculature and inhibits breast cancer metastases. Proc Natl Acad Sci U S A. 2013;110:E1291–1300. https://doi.org/10.1073/pnas.1220580110.
41. Fuchs K, Hippe A, Schmaus A, Homey B, Sleeman JP, Orian-Rousseau V. Opposing effects of high- and low-molecular weight hyaluronan on CXCL12-induced CXCR4 signaling depend on CD44. Cell Death Dis Nat Publishing Group. 2013;4:e819–819. https://doi.org/10.1038/cddis.2013.364.
42. Lisignoli G, Cristino S, Piacentini A, Cavallo C, Caplan AI, Facchini A. Hyaluronan-based polymer scaffold modulates the expression of inflammatory and degradative factors in mesenchymal stem cells: Involvement of Cd44 and Cd54. J Cell Physiol. 2006;207:364–73. https://doi.org/10.1002/jcp.20572.
43. Xu S, Xu H, Wang W, Li S, Li H, Li T, et al. The role of collagen in cancer: from bench to bedside. J Translational Med. 2019;17:309. https://doi.org/10.1186/s12967-019-2058-1.
44. Li X, Han H, Li S, Yang K, Yang Z, Ma L, et al. Cancer-associated fibroblasts: The Achilles' Heel in thyroid tumor progression and therapy. Cell Signal. 2026;138:112213. https://doi.org/10.1016/j.cellsig.2025.112213.
45. Naomi R, Ridzuan PM, Bahari H. Current Insights into Collagen Type I. Polym (Basel). 2021;13:2642. https://doi.org/10.3390/polym13162642.
46. Nigdelioglu R, Hamanaka RB, Meliton AY, O'Leary E, Witt LJ, Cho T, et al. Transforming Growth Factor (TGF)-β Promotes de Novo Serine Synthesis for Collagen Production. J Biol Chem. 2016;291:27239–51. https://doi.org/10.1074/jbc.M116.756247.
47. Hillege MMG, Galli Caro RA, Offringa C, de Wit GMJ, Jaspers RT, Hoogaars WMH. TGF-β Regulates Collagen Type I Expression in Myoblasts and Myotubes via Transient Ctgf and Fgf-2 Expression. Cells. 2020;9:375. https://doi.org/10.3390/cells9020375.
48. Furler RL, Nixon DF, Brantner CA, Popratiloff A, Uittenbogaart CH. TGF-β Sustains Tumor Progression through Biochemical and Mechanical Signal Transduction. Cancers (Basel). 2018;10:199. https://doi.org/10.3390/cancers10060199.
49. Perrin L, Belova E, Bayarmagnai B, Tüzel E, Gligorijevic B. Invadopodia enable cooperative invasion and metastasis of breast cancer cells. Commun Biol Nat Publishing Group. 2022;5:1–14. https://doi.org/10.1038/s42003-022-03642-z.
50. Velez DO, Tsui B, Goshia T, Chute CL, Han A, Carter H, et al. 3D collagen architecture induces a conserved migratory and transcriptional response linked to vasculogenic mimicry. Nat Commun Nat Publishing Group. 2017;8:1651. https://doi.org/10.1038/s41467-017-01556-7.
51. Li Q, Li M, Zheng K, Tang S, Ma S. Expression pattern analysis and drug differential sensitivity of cancer-associated fibroblasts in triple-negative breast cancer. Transl Oncol. 2021;14:100891. https://doi.org/10.1016/j.tranon.2020.100891.
52. Conklin MW, Eickhoff JC, Riching KM, Pehlke CA, Eliceiri KW, Provenzano PP, et al. Aligned collagen is a prognostic signature for survival in human breast carcinoma. Am J Pathol. 2011;178:1221–32. https://doi.org/10.1016/j.ajpath.2010.11.076.
53. Xi G, Guo W, Kang D, Ma J, Fu F, Qiu L, et al. Large-scale tumor-associated collagen signatures identify high-risk breast cancer patients. Theranostics. 2021;11:3229–43. https://doi.org/10.7150/thno.55921.
54. Jiang Y, Zhang H, Wang J, Liu Y, Luo T, Hua H. Targeting extracellular matrix stiffness and mechanotransducers to improve cancer therapy. J Hematol Oncol. 2022;15:34. https://doi.org/10.1186/s13045-022-01252-0.
55. Mai Z, Lin Y, Lin P, Zhao X, Cui L. Modulating extracellular matrix stiffness: a strategic approach to boost cancer immunotherapy. Cell Death Dis. 2024;15:307. https://doi.org/10.1038/s41419-024-06697-4.
56. Ribatti D, Tamma R, Annese T. Epithelial-Mesenchymal Transition in Cancer: A Historical Overview. Transl Oncol. 2020;13:100773. https://doi.org/10.1016/j.tranon.2020.100773.
57. Yu Y, Xiao C-H, Tan L-D, Wang Q-S, Li X-Q, Feng Y-M. Cancer-associated fibroblasts induce epithelial-mesenchymal transition of breast cancer cells through paracrine TGF-β signalling. Br J Cancer. 2014;110:724–32. https://doi.org/10.1038/bjc.2013.768.
58. Medici D, Nawshad A. Type I collagen promotes epithelial-mesenchymal transition through ILK-dependent activation of NF-kappaB and LEF-1. Matrix Biol. 2010;29:161–5. https://doi.org/10.1016/j.matbio.2009.12.003.
59. Hanahan D, Coussens LM. Accessories to the crime: functions of cells recruited to the tumor microenvironment. Cancer Cell. 2012;21:309–22. https://doi.org/10.1016/j.ccr.2012.02.022.
60. Garg P, Jallepalli VR, Verma S. Unravelling the CXCL12/CXCR4 Axis in breast cancer: Insights into metastasis, microenvironment interactions, and therapeutic opportunities. Hum Gene. 2024;40:201272. https://doi.org/10.1016/j.humgen.2024.201272.
61. Hassan AF, Kheraldine H, Abujamous L, Al-Thawadi H, Elhissi A. Inflammation-associated drug resistance and tumor growth in TNBC. Front Immunol. 2025;16:1623137. https://doi.org/10.3389/fimmu.2025.1623137.
62. Liao T, Chen X, Qiu F, Zhang X, Wu F, Zhao Z, et al. Regulation of cancer-associated fibroblasts for enhanced cancer immunotherapy using advanced functional nanomedicines: an updated review. J Nanobiotechnol. 2025;23:166. https://doi.org/10.1186/s12951-025-03217-0.
63. Mao X, Xu J, Wang W, Liang C, Hua J, Liu J, et al. Crosstalk between cancer-associated fibroblasts and immune cells in the tumor microenvironment: new findings and future perspectives. Mol Cancer. 2021;20:131. https://doi.org/10.1186/s12943-021-01428-1.
64. Ciavattone NG, Bevoor A, Farfel A, Rehman A, Ho KKY, Rock EC, et al. Inhibiting CXCR4 reduces immunosuppressive effects of myeloid cells in breast cancer immunotherapy. Sci Rep Nat Publishing Group. 2025;15:5204. https://doi.org/10.1038/s41598-025-89882-5.
65. Zhang M, Zhang B. Extracellular matrix stiffness: mechanisms in tumor progression and therapeutic potential in cancer. Exp Hematol Oncol. 2025;14:54. https://doi.org/10.1186/s40164-025-00647-2.
66. Han W, Chen S, Yuan W, Fan Q, Tian J, Wang X et al. Oriented collagen fibers direct tumor cell intravasation. Proceedings of the National Academy of Sciences. Proceedings of the National Academy of Sciences; 2016;113:11208–13. https://doi.org/10.1073/pnas.1610347113

Publisher's note